PERFORMANCE OF A LOW-FREQUENCY HIGH-FLOW ACOUSTIC SENSING ARRAY FOR TURBULENT OCEAN CONDITIONS

by

Eric Matthew Forsyth Auvinen

Submitted in partial fulfillment of the requirements
for the degree of Bachelor of Science

at

Dalhousie University
Halifax, Nova Scotia
April 2017

For my family

TABLE OF CONTENTS

LIST OF TABLES

LIST OF FIGURES

ABSTRACT

Baseline ambient sound level assessment is important in quantifying additional noise contributions from tidal energy infrastructure. Static acoustic sensing in high-flow conditions is complicated by pseudo-sound, or flow noise, generated by pressure fluctuations due to turbulent flow on the surface of a hydrophone. Signal processing methods are used to identify and suppress flow noise at low frequencies on a four-element horizontal hydrophone array with data collected in the Minas Passage in October, 2016. Observations of spectral slope and spatial coherence are used to track the masking effect of turbulence across frequency and flow speed, and identify the critical frequency threshold where flow noise exceeds the ambient noise. The array's performance in the Minas passage is quantified by an empirical relationship between current speed and the critical frequency. Beamforming, and coherent and incoherent averages are proposed as possible flow noise suppression methods and evaluated.

LIST OF ABBREVIATIONS AND SYMBOLS USED

Roman symbol	Description	Units
A	Spectral density of coherent array	Pa^2/Hz
AG	Array gain	dB re μPa
f	Frequency	Hz
G	Empirical spatial coherence threshold	Dimensionless
H	Histogram	Dimensionless
h	Bin width	dB re μPa
K	Coefficient	Dimensionless
L	Linear dimension	m
l	Number of elements on array	Dimensionless
M	Spectral slope	Dimensionless
m	Spectral slope between 10 Hz and 100 Hz	Dimensionless
N	Fourier transform of n	Pa·s
n	Flow noise component of sound field	Pa
NL	Noise level	dB re 1 μPa $\cdot$ Hz$^{-1/2}$
PSPD	Power spectrum probability density	Occurrences
Re	Reynolds number	Dimensionless
S	Power spectral density	Pa^2/Hz
ss	Sea state coefficient	Dimensionless
SNR	Signal-noise ratio	Dimensionless
T	Observation interval	s
U	Flow velocity	m/s
X	Fourier transform of x	Pa·s
x	Total output	Pa

Greek symbol	Description	Units
Γ	Coherence	Dimensionless
δ	Kronecker delta	Dimensionless
θ	Arrival angle	Radians
Σ	Fourier transform of σ	Pa·s
σ	Ambient component of sound field	Pa
τ	Acoustic travel time	s
υ	Kinematic viscosity	m^2/s
ω	Angular frequency	radian/s

ACKNOWLEDGEMENTS

Thank you to the *MV Nova Endeavour* crew, GeoSpectrum, and Black Rock Tidal Power Inc. for making this project a reality.

I am incredibly grateful for Dr. David Barclay giving me the chance to take on this project. His guidance, patience, and expertise made this entire process an absolute pleasure. I am extremely lucky that David was able to guide me through such a foreign and daunting task, and I believe that this thesis is a testament to his leadership and creativity.

CHAPTER 1

INTRODUCTION

The ambient sound field is defined as the noise field against which signals are detected (*Hildebrand*, 2009), and plays an important role in source characterization and ocean regime description. The military (*Gaul et al.*, 2007), scientific (*Barclay and Buckingham*, 2013), and industrial communities have all benefited from continuous improvements in ambient sound field characterization. More recently, ambient noise has been used in monitoring programs by the science and policy communities to assess the near-field and far-field impacts of anthropogenic noise (anthropophony) (*Smith and Pijanowski*, 2014). However, the utility of ambient sensing is considerably limited in turbulent ocean conditions, where pseudo-sound, or flow noise, is generated by pressure fluctuations on the surface of a hydrophone. The masking effects of flow noise can complicate source identification and background noise assessment in high-flow settings, such as tidal channels.

Flow noise suppression is necessary for reliable ambient sound field detection in high-flow settings. Flow shields and hydrophone housing, which can reduce the pressure fluctuations on the surface of a hydrophone, have been proposed as mechanical flow noise suppression methods. The present thesis explores the nature of flow noise in the low frequency range, and proposes a signal processing approach to flow noise identification, characterization, and suppression.

1.1 Ambient Noise

Ambient noise sensing facilitates meaningful anthropophony monitoring initiatives. In the absence of biological and anthropogenic sound sources (biophony, anthropophony),

the ambient sound field in the ocean is controlled by wind force, sea state, (*Wenz*, 1962) and other physical mechanisms such as rainfall (*Ma and Nystuen*, 2005) and snowfall (*Alsarayreh and Zedel*, 2011).

Ambient noise sensing is performed throughout the water column. Hydrophone positioning is important for signal interpretation, as the seafloor, sea surface, and bathymetric features can influence propagating noise (*Ingenito and Wolf*, 1989). Ambient sensing in high-flow settings presents a challenge, since sensors fixed to moorings and drifting buoys are subject to equipment-generated noise. For example, *Patrício et al.* (2009) identified moorings and other infrastructure as sources of abiotic noise in the ambient noise field. There are mechanical solutions to equipment noise, however these are only so effective.

Ambient noise monitoring is essential to environmental acoustic assessments (*Gordon et al.*, 2003) and source characterization (*Wenz*, 1962). Proper assessment of anthropophony requires reliable baseline ambient sensing. Information from baseline ambient acoustic testing provides the information necessary for noise pollution mitigation and passive acoustic monitoring (PAM) in regions of interest (*Hildebrand*, 2009). Industrial, military, and scientific groups have all benefited from improvements in acoustical source characterization. Indeed, meaningful source characterization provides insight on migratory marine species (*Dushaw et al.*, 2010), sea state (*Wenz*, 1962), seabed conditions (*Lombardi*, 2016), and weather (*Barclay and Buckingham*, 2013), all of which are difficult and expensive to actively observe, track, or monitor using conventional direct or in-situ methods.

Conventional ocean acoustics defines the low, medium, and high frequency bands as 10 Hz to 500 Hz, 500 Hz to 25 kHz, and > 25 kHz, respectively (*Hildebrand*, 2009). Propagating noise in the marine environment is strongly influenced by local ocean conditions and the physical characteristics of the sound source. Sound levels across frequency bands can provide insight on a variety of near-field and far-field sound sources. Ocean depth, wind speed, and water flow are all critical considerations in the marine acoustic environment (*Wenz*, 1962). The predictable influence of different conditions and processes can be used to identify, evaluate, and describe different sound sources using the ambient sound field. Surface waves, sediments (geophony), water droplets, biophony, anthropophony, and bubbles can all influence the ambient noise field. The deep ocean presents a highly unique acoustical setting, where the speed of sound can exceed 1600 m/s and physical conditions

present unique ambient fields (*Barclay and Buckingham*, 2013).

1.2   Background and Motivation

Tidal energy firms have acquired leases to sea floor space within the Minas Passage with aspirations of harnessing the high-flow currents typical of the region. Tidal energy is a contentious issue in Nova Scotia (*Gordon*, 1994), with many proximal stakeholders strongly opposing tidal energy development in the Bay of Fundy region (*Mulligan*, 2017). The potential near-field and far-field acoustical impacts of tidal turbine infrastructure are often cited by opponents of the the tidal turbine projects. Improvements in our understanding of the anthropophony associated with tidal turbine infrastructure are necessary if there is to be any tidal power development in the Bay of Fundy. However, the masking effects of flow noise make it difficult to reliably monitor the ambient sound field in high-flow tidal channels such as the Minas Passage.

The turbine industry is interested in establishing baseline ambient sound levels against which a site's anthropophony is to be measured. Proper flow noise suppression would facilitate reliable ambient noise monitoring, dramatically improving the effectiveness of passive acoustic monitoring programs. Furthermore, a signal processing algorithm solution could be more cost effective than a mechanical one.

Beyond industrial motivation, there is a clear academic significance to the suppression of turbulence-based flow noise. Currently, much of the underwater ambient literature has been focused on ambient sound-source characterization. However, the deterministic qualities of ambient sensing are reduced by flow noise, which masks the propagating noise. Flow noise can heighten signal power, steepen spectral slopes (*Bassett et al.*, 2014), and mask signals of interest at low frequencies. Furthering our ability to identify flow noise in ambient signals would extend our understanding of ambient noise fields. Additionally, an effective flow noise suppression technique would open up new settings for ambient sensing.

1.3   Objectives

Successful suppression of flow noise could benefit passive acoustic monitoring systems in the tidal energy sector. Additionally, improved ambient sensing in high-flow conditions

would improve our understanding of underwater ambient sound fields. As such, the main objectives of the following research are:

1. Use spectral analysis and spatial coherence to identify and characterize flow noise at low frequencies.

2. Use beamforming and coherent averaging to improve the performance of the array by suppressing flow noise and enhancing the measurement of ambient noise.

CHAPTER 2

LITERATURE REVIEW

2.1 Ambient Noise

Interest in the ocean's low frequency ambient noise field started when the U.S. Navy began using signal processing as means of ship and submarine detection. Indeed, early researchers found ways to extract and identify natural and human-based components of the ambient noise field. Recent work has focused on anthropophony in the ocean, both in terms of noise contributions and frequencies of influence (*Lombardi*, 2016). Shipping, recreational boating, moorings, and cities are known to affect the ambient noise fields of the ocean (*Hildebrand*, 2009). Other sources of sound in the ocean include wind, surface waves, water droplets, marine life, and bubbles (*Prosperetti*, 1988). Accurate statical characterization of the ambient noise field has facilitated the optimization of acoustic array design, such that coherent averaging across the array can be used to reject uncorrelated noise and enhance signals (*Jensen et al.*, 2000).

2.2 Sources of Noise

The ambient noise field is composed of a multitude of biotic and abiotic sources of sound. Most sources of sound are interrelated and co-occurring, such as wind and waves, and vary on temporal and spatial scales.

2.2.1 Bubbles

Bubbles play an important role in oceanic ambient noise, and are primarily active from a few Hz to several kHz (*Prosperetti*, 1988). Bubbles are found in the water column when

wind is low, high, or even absent (*Wenz*, 1962). Surface bubble-sourced noise is elevated during periods of increased wind and wave action. Other surface sources of bubbles are biology, sea-spray, rain, and splashes (*Prosperetti*, 1988). Bubbles are generated at depth by decaying matter, fish belches, and seafloor gas emissions (*Wenz*, 1962). Bubble signatures can be masked by far-field sound sources such as shipping and explosions at low frequencies.

Bubbles generate noise through two distinct mechanisms: oscillation, and cavitation. Newly formed bubbles will contain some initial mechanical energy (*Prosperetti*, 1988), some of which is translated to noise through damped oscillations induced by pressure fluctuations within the water column. The acoustic waves generated by bubble oscillations correspond to the natural frequency of the emitting bubble, which is inversely proportional to bubble size (*Minnaert*, 1933). Rising bubbles are affected in a similar fashion, where the changes in hydrodynamic pressure generate bubble oscillations and acoustic waves. Bubble cavitation involves both the formation and collapse of air bubbles within the ocean. Bubble collapse is a substantial component of underwater ambient noise fields, and contributes to the wind-dependence of underwater spectra.

Surface-originating bubbles generate acoustical signals that preferentially propagate in a vertical direction due to their proximity to the sea surface. Bubble oscillations can add meaningful levels of noise to the ambient field, and have been known to influence ambient environments over considerable distances (*Wenz*, 1962).

Prosperetti (1988) identifies three distinct ambient regions heavily influenced by bubble populations within the underwater environment. At frequencies below 200 Hz, bubbles amplify pressure fluctuations generated by turbulent flowing water. This suggests there is a synergistic relationship between bubble acoustical mechanisms and the sound generated by turbulent flows. Single-bubble oscillations are prevalent in the ambient sound field in the kHz frequency band. At intermediate frequencies, oscillating bubble clouds are a sizable component of the underwater noise field. Beyond these frequencies, rain-derived bubbles can be influential (*Prosperetti*, 1988). Bubbles affect both the shape and levels of ambient sound fields across a wide range of frequencies, and the effects of bubble populations are present throughout the ambient spectra. Bubble action is tightly linked to biophony, turbulence, anthropophony, wind, waves, precipitation, and other hydrodynamic processes (*Wenz*, 1962).

2.2.2 Wind and Sea State

The wind component of the underwater ambient noise field is a combination of oscillating bubbles and breaking surface waves (*Knudsen et al.*, 1948). *Carey and Browning* (1988) reviews empirical evidence of wind-dependence within the ambient noise spectrum, highlighting the depth dependence of wind-generated noise. Bathymetry is an important factor in wind-dependent sound fields (*Carey and Browning*, 1988). Noise below the critical depth depends more on local winds, while noise at the sound channel axis depends on both local winds and distantly generated wind noise (*Barclay and Buckingham*, 2013). Primary wind-dependence within the ambient sound field occurs between 100 Hz and 25 kHz (*Wenz*, 1962), with the potential for noise contamination by far-field sources (such as industrial activity) between 10 Hz and 1 kHz. The uncertainty in early technology made precise and accurate deep ocean ambient source characterization difficult, however technologies have improved considerably.

Cato (2008) suggests that wind-generated noise is more dependent on the bubbles generated by entrainment than the wave action induced by wind-sourced momentum fluxes. Therefore, while sea state agitations are a crucial component of the underwater noise field, it would seem that bubbles play a greater acoustical role.

Sea state fluctuations are an important source of wind-generated ambient sounds. Breaking waves have been repeatedly observed as a substantial component of the oceanic ambient sound field. Fluctuations in sea state generate subsurface pressure fluctuations which affect underwater ambient sensing systems (*Wenz*, 1962). According to *Knudsen et al.* (1948), wind and wave components of ambient spectra follow

$$\text{NL} = 56 + 19\log(ss) - 17\log f \qquad (2.1)$$

where ss is the sea state ($1 < ss < 6$), f is frequency ($1 < f < 25$ kHz), and NL is the noise level in a 1 Hz bin. The units of equation 2.1 are in dB re 1 μPa $\cdot$ Hz$^{-\frac{1}{2}}$ (*Hildebrand*, 2009).

Wind-generated sea surface fluctuations elevate underwater ambient noise levels (*Hildebrand*, 2009) and generate both first-order and second-order pressure fluctuations (*Wenz*, 1962). First-order pressure fluctuations are attenuated with depth according to their frequency. This depth dependence results in a considerable drop-off of wind and surface wave

sound components in ambient noise fields at depth. Conversely, second-order pressure fluctuations, generated by waves of equal wavelength and opposite in direction, are not attenuated with depth and contribute to low-frequency ambient noise fields.

Knudsen et al. (1948) identified sea-surface motion components of underwater ambient noise at mid-frequencies. Sea-state sound sources, including waves and bubbles, overwhelmingly follow a -17 dB per decade spectral slope and have been repeatedly observed. The ambient noise influence of surface waves can be masked by unrelated near-field and far-field sounds (*Hildebrand*, 2009). Surface-generated noise radiates downward with cosine directionality because the sources are near the surface, which acts as an acoustic mirror, thus creating a dipole source directionality (*Hildebrand*, 2009). Our understanding of wind-dependence in the ambient noise field has allowed for significant progress in source characterization. *Vagle et al.* (1990) is a good example of this, where noise levels are used to measure wind speed.

2.2.3   Precipitation/Water Droplets

The main sources of underwater sound from splashes are: droplet impact, droplet oscillation, and volume pulsations (*Franz*, 1959). Droplet-generated noise is proportional to a droplet's radius and impact velocity, and the resulting sound pulsations are cosine in direction. The ambient field is heavily influenced by droplet impacts when entry velocity is high, and is dominated by entrained air bubble noise at low entry velocities (*Franz*, 1959). Surface splash acoustic waves are a product of randomly spaced transient sounds from a population of droplet impacts (*Franz*, 1959). It is important to note that bubble-droplet co-occurrence can alter the acoustical signals of individual droplets (*Wenz*, 1962). *Franz* (1959) suggests that water droplet spectra shape and power are controlled by droplet size, shape, velocity, and density. Moreover, the most influential acoustical variables are entrance velocity and droplet size.

Water droplets and splashes typically occur in dynamic settings, such as rainstorms, whitecap conditions, or high-wind events. Furthermore, water droplets can produce other sound-sources such as bubbles and surface agitation. This co-existence makes the identification and characterization of water droplet noise relatively challenging, particularly in an open ocean setting. Impacts of water droplets affect a broad range of frequencies in the kHz range (*Franz*, 1959), where the bubble portion of water droplet impacts yield spectral peaks between 1 and 10 kHz within the ambient noise field. Together, water

droplet impacts and the ensuing bubbles affect mid-to-high frequencies, although they can be influential at frequencies as low as 100 Hz (*Wenz*, 1962). Precipitation behaves similar to water droplets in the ambient field, where its effects are most noticeable above 500 Hz (*Wenz*, 1962). Rain, hail, and snow, each exhibit distinct acoustical effects. Rainfall rates and snowfall characterization from ambient noise have been demonstrated by *Ma and Nystuen* (2005) and *Alsarayreh and Zedel* (2011), respectively.

2.2.4 Biophony

The underwater ambient sound field is endlessly bombarded by sound waves from marine mammals, invertebrates, and other life. Tidal channels are no exception, and are home to a diverse crowd of biological sound sources. Ambient biophony is variable, changing with the presence of different species and taxa, along with biodiversity and species richness. Fishes contribute a considerable amount of noise to the ambient environment, particularly between 100 and 500 Hz. There are substantial fish populations in the Minas Passage (*Dadswell*, 2010), some of which are known to produce sound (*Wilson et al.*, 2004). Fish are not only a significant individual sound source, but groupings of fish can generate choruses of low-frequency noise which elevate sound fields by 20 to 30 dB. Fish generate sound waves through two separate mechanisms: stridulation and muscle action (*Hildebrand*, 2009). Stridulation generates broadband pulses, while noise produced by muscle convulsions are pulsed tonals (*Hildebrand*, 2009).

Marine mammals are another significant component of underwater ambient noise fields, particularly in the Minas Passage. Pilot whales, dolphins, and seals all frequent the Minas Passage and Minas Basin (*Tollit et al.*, 2011) and would be an important component of the ambient environment. Mammals generate sounds through cries, moans, barks, grunts, cracklings,clicks, and whistles (*Wenz*, 1962). Whales generate noise over incredibly large distances using deep sound channels, and communicate through repeated moans. The frequency and power range of marine mammal vocalization varies across species and taxa. Thse vocalizations exhibit varying duration, levels, and repetition. Whales and other marine mammals have developed sophisticated communication and echolocation systems, making the ambient noise field essential to their ecological success (*Hildebrand*, 2009). Due to the mobility of marine mammals, their biophony contributions vary with time and space and are therefore difficult to predict (*Wenz*, 1962).

Beyond mammals and fishes, the Minas Passage is home to a diverse group of noisy

vertebrates and invertebrates. Sharks, mussels, clams, lobsters, crabs, shrimp, and other animals could all contribute to local sound levels. Proper characterization of Bay of Fundy ambient noise fields would require the consideration of all these sound sources. The dynamic nature and inherent variability associated with tidal channel ecosystems makes reliable source identification and characterization incredibly challenging.

2.2.5 Anthropophony

A large part of the motivation behind underwater ambient noise sensing is the monitoring of anthropogenic sound sources, or anthropophony, in tidal channels. Cities, boats, swimmers, and infrastructure all add noise to the underwater environment. Ship noise is the near-field noise from vessels in the ocean, and can heavily influence ambient sound levels. *Wenz* (1962) reports narrow band ship noise at frequencies below 1 kHz, as well as less prevalent effects in the kHz region. Ocean traffic noise is defined as the culmination of vessel traffic in the ocean, varying with transmission loss, number of ships, and ship distribution (*Wenz*, 1962). Traffic noise changes with ship type, and is particularly influential between 20 and 500 Hz. Vessel traffic noise is important in the open ocean, and the depth of the Minas Passage would limit the prevalence of traffic noise.

Industrial activities are an important source of anthropophony in the ocean. Oil drilling, pile driving, wind farms, and acoustic telemetry are all stationary industrial sound sources. Drilling, pile driving, and wind turbines are sources of low-to-medium frequency noise capable of significantly elevating near-field sound levels (*Hildebrand*, 2009). Telemetry is widely used for underwater communications and data transfers, and generates noise over long distances at high frequencies. Moorings and infrastructure installations are another source of industrial noise (*Patrício et al.*, 2009). The anthropophony contributions of tidal turbines and tidal turbine infrastructure in tidal channels is not well understood. *Khan et al.* (2009) presents an overview of tidal turbine technology, and suggests that blade orientation can influence a turbine's sound levels. While there lacks any in-situ studies of turbine anthropophony, it is not unreasonable to expect tidal turbine infrastructure to generate meaningful levels of noise.

Other sources of anthropogenic noise include explosives, acoustic deterrent devices, acoustic harassment devices, sonar, and underwater vehicles. Explosions generate elevated broadband signals that can greatly influence the near-field and far-field ambient environments, with pronounced impacts at low frequencies (*Hildebrand*, 2009). Acoustic deterrent

and harassment devices are used to deliberately pollute near-field ambient environments to avert local biota. Sonar and other acoustical devices emit mid-to-high frequency noise, however the frequency of influence varies with the device/system (*Hildebrand*, 2009).

A primary motivation behind the study of anthropophony is the assessment of its impact on local biology. There is concern that anthropophony negatively impacts marine mammals and other marine life. There is reason to be believe that the communication, detection, and navigation abilities of whales, fish, and other animals can be complicated by propagating anthropophony within the water column (*Lombardi*, 2016). *Halvorsen et al.* (2011) demonstrates the adverse physiological effects tidal turbine noise has on fish. Conversely, (*Croll et al.*, 2001) shows that continuous and increasing low-frequency anthropophony had no visible effect on foraging whales. *Bailey et al.* (2010) identifies pile driving as a potentially harmful sound source, however there are ways to mitigate this noise pollution. Quite clearly the implications of anthropophony are undecided, and the difficulty of measurement and close observation have not helped improve our understanding. Anthropophony levels, duration, and frequency present potential ecological, biological, and environmental risks that require investigation in future studies.

2.3 Flow Noise

Analogous to the turbulent air flow pseudo-sound described by *Lighthill* (1962), flowing water in a high Reynolds number regime ($Re >> 1$, flow is fast relative to long axis of submerged object) generates pressure fluctuations on the surface of a hydrophone. These pressure fluctuations produce flow noise, or pseudo-sound, which is irregular, uncorrelated, and inherently stochastic. The Reynolds number is defined as

$$Re = \frac{UL}{v}$$

(2.2)

where U and L are the velocity and length scales of the flow, and v is the kinematic viscosity of the fluid (*Van Dyke*, 1982).

Local pressure fluctuations on the surface of a hydrophone represent near-field turbulence (*Strasberg*, 1979). Hydrophones moving with the mean flow will detect very little flow noise, as it is the *relative* flow of water over a hydrophone's surface that causes pressure fluctuations and pseudo-noise.

Turbulent flows occupy a wide range of frequencies and wavenumber domains, with broad spatial and temporal variability. The advective nonlinearity and sensitivity of turbulent flows make them unpredictable in space and time. This nonlinearity contributes to the chaotic and complex systems within turbulent flows. (*Van Dyke*, 1982). While turbulence is governed by classical mechanics and known cascade laws, the flow and its resulting pseudo-sound are hard to predict.

The spectral components of flow noise have been casually identified, however the degree of variability in each signal makes rigorous mathematical description exceedingly difficult. *Lombardi* (2016) reports steepened spectral slopes in a high-flow regime, an artifact of small-scale turbulence on the submerged sensor. This steep spectral slope, f^{-m}, has been the subject of modelling and characterization studies (*Bassett et al.*, 2014). A spectral slope of $f^{-5/3}$, analagous to Kolmogorov's turbulence theory, is reported at frequencies below 10 Hz. This slope is not to be confused with the coincidental wind-generated slope of the same value, which occurs at higher frequencies (*Knudsen et al.*, 1948).

Flow noise presents a unique challenge for passive acoustic monitoring: a hydrophone in a high-flow regime will record both propagating noise and pseudo-noise. This suggests that models and formulations should distinguish between the two sound sources in order to properly evaluate ambient signals. *Barclay and Buckingham* (2013) details a signal processing approach to flow noise suppression in deep ocean ambient signals, involving spectral analysis and spatial coherence. Beyond this mathematical approach, mechanical/engineered solutions such as flow shields and unique hydrophone design can be used to suppress pressure fluctuations on the surface of a hydrophone. However, these solutions are relatively unrefined untested.

CHAPTER 3

MATERALS AND METHODS

3.1 Site Description
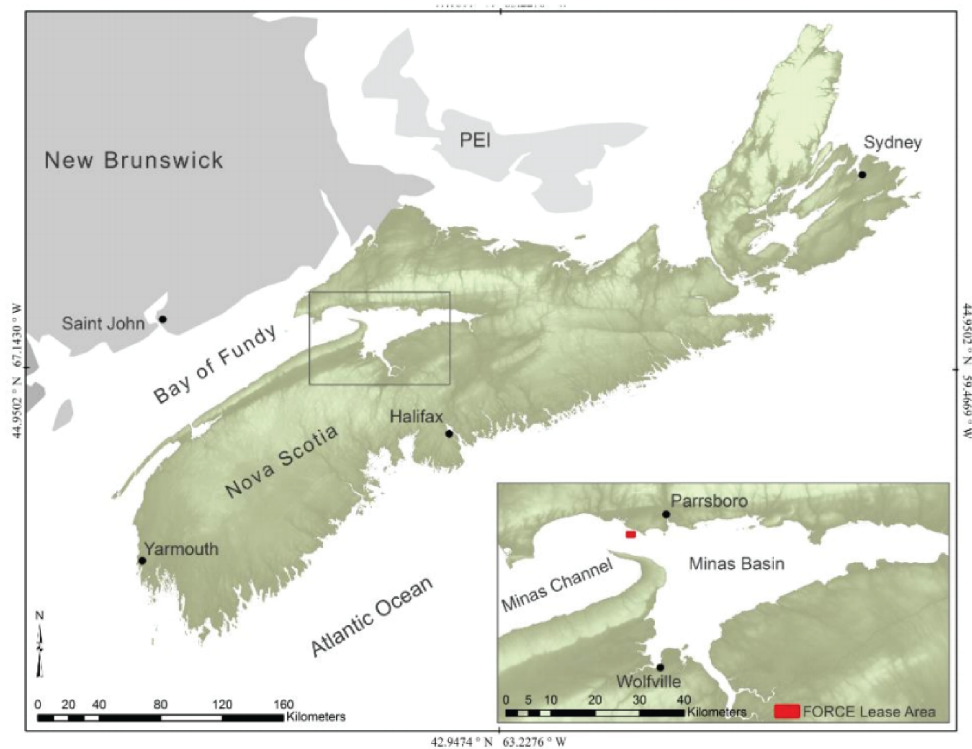

Figure 3.1: Experiment location; Minas Passage, a tidal channel, adapted from *Morrison and Redden* (2012).

The Bay of Fundy and its strong tidal currents have attracted several prospective tidal power firms. The Bay boasts some of the largest tides in the world, reaching amplitudes of 18 meters at the head of the Bay and 6 meters in the Minas Basin (*Karsten et al.*, 2008).

13

The Minas Passage (Figure 3.1) is a narrow tidal channel which connects the Minas Basin to the rest of the Bay (*Shaw et al.*, 2012), and is characterized by particularly vicious currents. The natural period of the Bay of Fundy is fairly close to the dominant regional semi-diurnal tide (12.42 hours per cycle) (*Karsten et al.*, 2008). This relative resonance is the mechanism responsible for the anomalous tides in the Bay of Fundy.

The Fundy Ocean Research Centre for Energy (FORCE) has established a test site for tidal technology in the Minas Passage in hopes of bringing together the industrial, policy, and scientific communities (*Shaw et al.*, 2012). Several studies have taken place at the FORCE site, describing the local geology, biology, and physical characteristics.

The Minas Basin and Passage are surrounded by high, undercut cliffs, which have long been exposed to aggressive erosion and are relatively unstable. On the Southern shore of the Passage, Cape Split acts as a barrier to swells, leaving wind as the primary source of waves in the Passage (*Wilson*, 2016).

3.2 Data Collection

3.2.1 Field Work

Field work was completed on October 27th, 2016, in the Minas Passage of the Bay of Fundy. The deployment period spanned roughly four hours, from 12:00 ADT to 16:00 ADT. This experimental window was chosen in order to capture the transition from maximum ebb tide to slack tide. This allowed for an observation of the local ambient environment in a variable current regime.

At 15:45 ADT tidal currents began to slack and both the guard buoy and array were powered off. Data was downloaded off of the guard buoy as the vessel steamed for Parrsboro, and the experimental data was lifted off of the experiment computer.

3.2.2 Array

A linear 4 element array (Figure 3.2) was deployed for the duration of data collection period. The array was constructed by GeoSpectrum, and contains 4 sequentially spaced hydrophones with a horizontal configuration (Figure 3.3). Each hydrophone pair is separated by 17 centimeters such that the maximum spacing is 51 centimeters. The array hydrophones were set to sample at a rate of 96.038 kHz with an acoustic bandwidth of 48.019 kHz. The array was towed from the *MV Nova Endeavour* (42' x 16'), which was

anchored to the seafloor in the Minas Passage. The four channels on the array continuously recorded 10 minute WAV files over a 4 hour period. The elements of the array were sampled simultaneously, allowing for coherent processing.
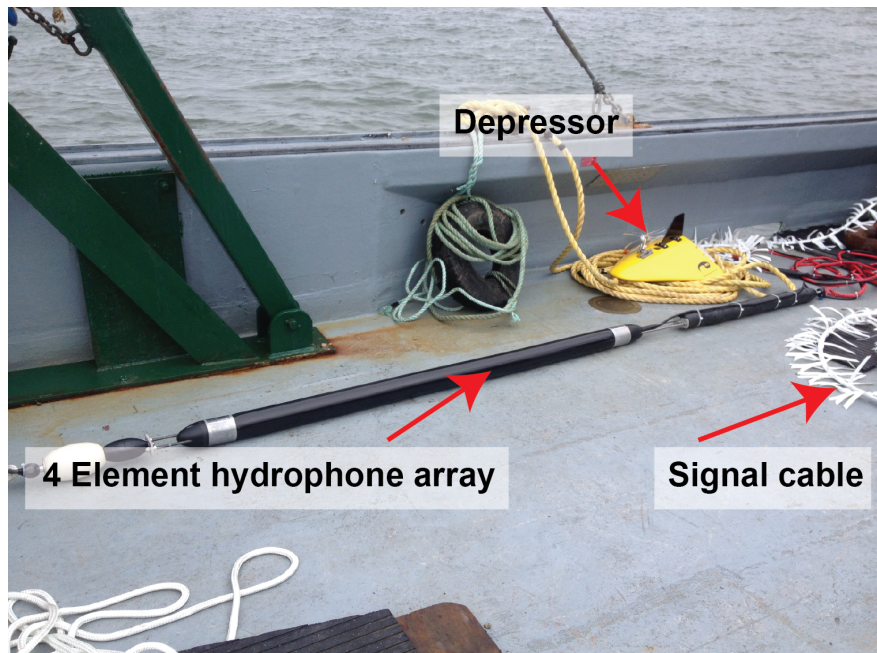

Figure 3.2: Photo of acoustical array and depressor used in experiment. Equipment is labeled.

The linear array was assembled on site and positioned 15 meters below the sea surface using a depressor/tow-fish. Linear array signals were transferred to the *MV Nova Endeavour* using a signal cable and were subsequently processed by an analog-to-digital converter (ADC). The signal cable was attached to the tow cable (6GA galvanized wire) using cable ties, and carried both the array and a drogue. The signal cable was sheathed in a fairing to reduce strum generation. Live signals were analyzed on-site to monitor array performance and ensure that the equipment was functioning properly.

The array elements recorded raw signals in units of counts. The power spectra/spectral density of these readings were calibrated according to the frequency-dependent array sensitivities. The calibrated units of power are in dB re 1 μPa.

3.2.3   Drifting Hydrophone

The drifting hydrophone (guard buoy) was deployed using a small auxiliary vessel launched from the *MV Nova Endeavour*. The guard buoy was suspended at a depth of $\sim$ 1 meter
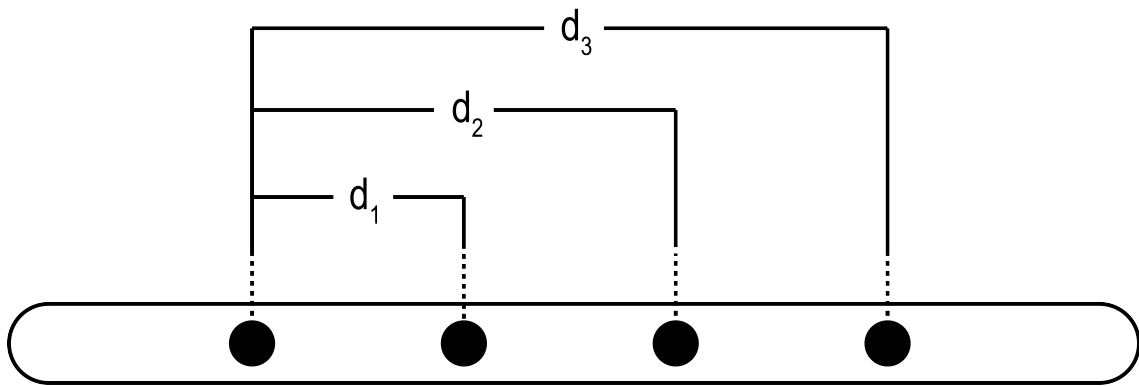
Figure 3.3: Schematic view of linear array. Hydrophones are shown, as well as the corresponding separation distances. d_1 is 17cm, d_2 is 34cm, and d_3 is 51cm.
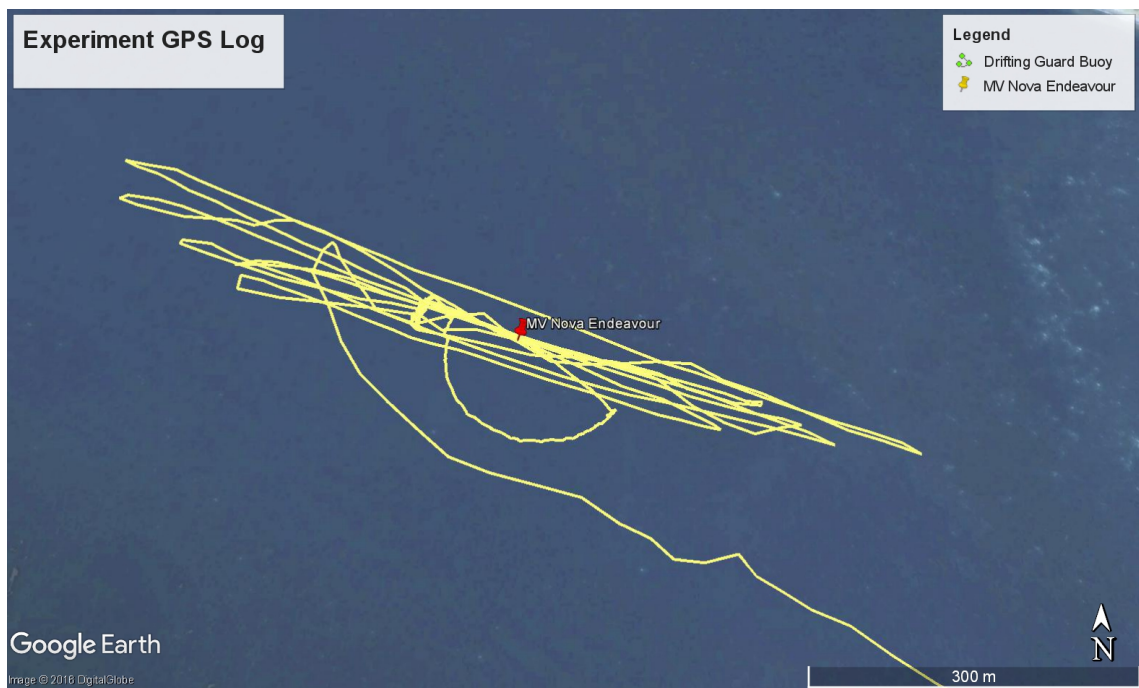

Figure 3.4: GPS tracks of drifting guard buoy and *MV Nova Endeavour* over the deployment period. Green line is the guard buoy track, and blue track is the main vessel.

using a drifting float and isolation system made of spectra and compliant bungee. The system isolated the recording hydrophone and instrument package from any surface action, such as the vertical movement of waves, which would otherwise generate instrument or flow noise. The guard buoy was positioned upstream by the author and an *MV Nova Endeavour* crew member in a rigid-hulled inflatable boat (RHIB). A total of five transects were performed by driving the guard buoy upstream, deploying the drifter, then floating downstream in the RHIB alongside the guard buoy until ~ 50 feet past the array. These transects were performed over the course of three hours, beginning at 13:00 ADT. The GPS visualization of these transects is presented in figure 3.4.

The guard buoy sampled at a rate of 96 kHz with an acoustic bandwidth of 48 kHz, and was fitted with a GPS to record transect geospatial information. The guard buoy is 79 centimeters in length and 14 centimeters in diameter. The guard buoy recorded WAV files in 30 minute segments and saved them to its 512 GB hard drive. The guard buoy model used in the experiment is shown in figure 3.5

Figure 3.5: Photo of the guard buoy model deployed during experiment.

Similar to the linear array, the guard buoy records raw signals in units of counts. The

corresponding power spectra were calibrated according to the frequency-dependent guard buoy sensitives, yielding dimensions of dB re 1 μPa. The guard buoy signals are (ideally) flow noise free and were used as benchmarks to assess the performance of the array. During transects the auxiliary vessel drifted with guard buoy with its engines off, and the guard buoy was retrieved at the transect terminus when it was in close proximity to the array.

3.2.4 Physical Conditions

Wind speed was measured intermittently throughout the deployment period using a hand-held wind speed gauge (Table 3.1). WebTide's predictive models were used to gather relevant water level and flow speed data. Surface conditions remained constant during the experiment. The presence and approximate location of other vessels was noted in the log book.

Table 3.1: Wind speed measurements taken over the deployment period.

Time (ADT)	Wind speed (m/s)
13:35	4.9
14:35	5.2
15:00	6.2
15:10	6.2
15:35	4.2
15:48	3.2

3.2.5 Notable Events

Important events throughout the experimental period are summarized in table 3.2.

Table 3.2: Notable experiment events with their timestamps.

Time (ADT)	Event
12:15	The boat is 'swaying' in the current, dragging the array line across the deck. Tow line is tied off to sides of the boat to reduce dragging.
13:22	The noise floor is $\sim$ 70 dB $>$ 1kHz, which is relatively high. Experiment gear is rearranged and reconfigured, depth sounder is powered off, and the boat engine is cut.
14:06	Lobster boat passed between us and land $\sim$ 200m on port side.

3.3   Data Analysis

Data analysis was performed in MATLAB in several stages. The analysis began with the calculation of the power spectral density (PSD) from the raw WAV files, followed by spectral analysis, spatial coherence, and beamforming. Visual assessment of the signal processing results provided direction for flow noise identification and characterization. Furthermore, rigorous quantitative evaluation of the results facilitated further description of the flow and ambient noise recorded during the deployment period.

3.3.1   General Signal Processing

Here, the output of a hydrophone is defined as

$$x_i(t) = \sigma_i(t) + n_i(t) \tag{3.1}$$

where x_i is the recorded time series on each ith hydrohpone, σ_i is the sound field's ambient components, and n_i is the locally generated flow noise. Importantly, n_i and σ_i are uncorrelated. Furthermore, the inherent randomness of flow noise makes n_i incoherent with respect to n_j.

The power spectrum, or spectral density, is defined as

$$S_{ii}(\omega) = \frac{\langle X_i(\omega) \cdot X_i^*(\omega)\rangle}{T} \tag{3.2}$$

where X_i is the Fourier transform of x_i, ω is angular frequency, * denotes a complex conjugate, and $\langle\rangle$ indicates an ensemble average, and T is the observation interval. All Fourier transforms are windowed by a Hann function. The Fourier transform is 2^{16} points long and contains 99 degrees of freedom.

Coherence is used to quantify the similarity between two signals. Here, coherence is defined as

$$\Gamma_{ij}(\omega) = \frac{S_{ij}(\omega)}{(S_{ii}(\omega) \cdot S_{jj}(\omega))^{\frac{1}{2}}} \tag{3.3}$$

3.3.2 Power Spectrum Probability Density

Spectral probability density (SPD) is an analytical technique used to depict a power spectrum. The SPD is used to depict the variability of the power spectrum over a period that is much longer than the minimum time required for a stationary measurement of power to be made. This form of analysis facilitates the identification of unique events within a series of spectra (from macro-scale). This thesis uses a modified version of the spectral probability density framework developed in *Merchant et al.* (2013). The power spectrum probability density (PSPD) is defined as

$$\text{PSPD}(f) = H(S_{ii}(f), h) \tag{3.4}$$

where $\text{PSPD}(f)$ is the power spectrum probability density at frequency f, and $H(S(f), h)$ is the histogram of the power spectrum S_{ii} at frequency f with a histogram bin width of h dB re 1 μPa. By combining PSPD results across frequencies, we can generate a PSPD matrix

$$\begin{bmatrix} \text{PSPD}(f_1) & \text{PSPD}(f_2) & \text{PSPD}(f_3) & \ldots & \text{PSPD}(f_a) \end{bmatrix} \tag{3.5}$$

where $\text{PSPD}(f_a)$ is the PSPD at the ath frequency.

3.3.3 Spectral Slope Threshold

Lombardi (2016) and *Bassett et al.* (2014) suggest that there are three distinct spectral slope regions in the low-to-mid-frequency range: at < 10 Hz spectra follow Kolmogorov's $f^{-5/3}$ spectral slope, at $10 < f < 100$ Hz, spectral slopes correspond to f^{-m} due to small-scale turbulence flow noise interacting with the finite size of the sensor surface (*Bassett et al.*, 2014), and at $f >\sim 100$ Hz, spectral slopes are determined by near-field and far-field ambient sound sources.

Any given spectral slope is defined as

$$f^{-M} = \frac{S_{ii}(2\pi f_a) - S_{ii}(2\pi f_b)}{\log(f_a \cdot f_b^{-1})} \tag{3.6}$$

where $S_{ii}(2\pi f_a)$ is the spectral density on the ith sensor at frequency f$_a$ and $S_{ii}(2\pi f_b)$ is the spectral density on the ith sensor at frequency f$_b$. Equation 3.6 describes the spectral slope in dB/decade. f^{-m} from *Bassett et al.* (2014) is found using equation 3.6 between 10 Hz and 40 Hz ($a = 10$ Hz, $b = 40$ Hz).

The transition from the flow noise region of f^{-m} to the ambient noise region is marked by the 'frequency knee', where the spectral slope begins to shallow. That is, the exit from the flow noise region is marked by a deviation below the slope f^{-m}. Thus, critical frequency, f_c, is defined as the first frequency at which

$$|f^{-M}| < |f^{-m}| \tag{3.7}$$

is true.

3.3.4 Spatial Coherence Threshold

Spatial coherence is calculated for each channel combination using equation 3.3, providing an assessment of signal similarity between elements. Propagating ambient noise is highly correlated across the array. Additionally, propagating noise at wavelengths sufficiently large relative to element spacing produces very high coherence (approaching $\sim$ 1) at low frequencies by effectively co-locating sensors. Conversely, flow noise generates considerable incoherence as pseudo-sound is inherently stochastic and uncorrelated across the linear array. Therefore, in the band f ¡ 500 Hz, flow noise is marked by low coherence while ambient noise is marked by high coherence. The transit of this coherence boundary, from flow noise (incoherent) to ambient noise (coherent) provides a metric for describing the extent of flow noise across the array.

The spatial coherence critical frequency, f_c, is defined as the frequency at which a minimum coherence threshold is crossed. Record length, hydrophone spacing, and other physical details suggest a reasonable spatial coherence threshold range of 0.7 - 0.9.

Formally, f_c is the first frequency at which

$$|\Gamma_{ij}(\omega)| \geq G_{ij} \tag{3.8}$$

where G_{ij} is the empirical spatial coherence threshold. Here, the threshold ranges between 0.7 and 0.9. This second critical frequency method is known as 'spatial coherence thresholding'.

3.3.5 Linear Regression

Both spectral slope and spatial coherence critical frequency distributions are related to their respective flow speeds (obtained from WebTide). A linear regression between critical

frequency, f_c, and flow speed, u, is used to identify and characterize the prevalence of the flow noise and ambient noise regions. Importantly, no data points are excluded from this regression.

3.3.6 Beamforming

Coherent beamforming is used to suppress spatially uncorrelated values and enhance the measurement of propagating ambient noise. This thesis uses a broadside beamformer coherently average the channels across the array. Ideally, this process suppresses stochastic values and enhances correlated terms. Locally generated flow noise and the ambient sound field are inseparable, however we can describe their relative prevalence with the theoretical signal-noise ratio (SNR). By taking the Fourier transform of equation 3.1 and substituting into equation 3.2, we find

$$S_{ii} = \frac{\langle X_i(\omega) \cdot X_i^*(\omega) \rangle}{T} \tag{3.9}$$

$$S_{ii} = \frac{\langle (\varsigma_i + N_i) \cdot (\varsigma_i^* + N_i^*) \rangle}{T} \tag{3.10}$$

where ς_i and N_i are the Fourier transforms of σ_i and n_i, respectively. For clarity, the frequency dependency, ω, has been omitted. Note that ς_i and N_i are uncorrelated, so we can expand equation 3.10 to arrive at

$$S_{ii} = \frac{\langle \varsigma_i \varsigma_i^* \rangle + \langle N_i N_i^* \rangle}{T} \tag{3.11}$$

Given equation 3.11, the SNR for a single hydrophone (SNR$_H$) is defined as

$$\text{SNR}_H = \frac{\langle \varsigma_i \varsigma_i^* \rangle}{\langle N_i N_i^* \rangle} \tag{3.12}$$

where SNR$_H$ = 1 at the critical frequency, f_c. Equation 3.12 applies to single hydrophone sensors. Now consider an array of hydrophones indexed by i, where the ambient sound field component of the signal on each phone is

$$\sigma_i(t) = \sigma_1(t - \tau_{i-1}) \tag{3.13}$$

where

$$\tau_i = \frac{d_i \cdot \cos\theta}{c} \tag{3.14}$$

is the acoustic travel time in seconds, for plane wave noise arriving on the sensors at the angle θ. Here, d_i denotes the separation distance between the first and ith hydrophone (Figure 3.3). Taking the Fourier transform of equation 3.13 gives

$$\varsigma_i(\omega) = \varsigma_1(\omega)e^{-i\omega\tau_{i-1}}. \tag{3.15}$$

The coherent sum of the signals on each element, with no time delay, is defined as

$$x_T(t) = \sum_{i=1}^{l} x_i(t) \tag{3.16}$$

where $x_i(t)$ is the signal recorded on the ith element of a linear array l elements long. $x_T(t)$ is the equivalent to beamforming broadside to the array. Since the source of interest is ambient noise, the sound field is assumed to be axially symmetric. Thus the horizontal array orientation and beam direction are unimportant, provided an appropriate array gain compensation is applied. The Fourier transform of equation 3.16 is

$$X_T(\omega) = \sum_{i=1}^{l} X_i(\omega). \tag{3.17}$$

The array power spectral density can be estimated using equation 3.17 by

$$A = \frac{\langle X_T(\omega) \cdot X_T^*(\omega) \rangle}{T}. \tag{3.18}$$

Given an array with both ambient noise and flow noise components, equation 3.17 can be expanded to

$$X_T = [\varsigma_1 + N_1 + \varsigma_2 + N_2 + \ldots \varsigma_l + N_l] \tag{3.19}$$

which describes the total output of all sensors on an array with l elements. Substituting equation 3.15 into equation 3.19 gives

$$X_T = \varsigma_1 + N_1 + \sum_{i=2}^{l}(\varsigma_1 e^{-i\omega\tau_{i-1}} + N_i).$$ (3.20)

Using the Fourier transform of the coherently summed outputs across the array, the power spectral density can be computed by substituting 3.20 into equation 3.18 yielding

$$A = \frac{\langle \varsigma_1\varsigma_1^* \left[l + \sum_{i=1}^{l-1} \frac{1}{2}\left(l - i\right)cos(\omega\tau_i)\right] + N \cdot N^* \rangle}{T}$$ (3.21)

where

$$N = \sum_{i}^{l} N_i$$ (3.22)

is the coherently summed flow noise. This term can be simplified by assuming the power of the flow noise measured on each individual hydrophone is equal across the array,

$$\langle N_i N_i^* \rangle = \langle N_j N_j^* \rangle$$ (3.23)

and uncorrelated between the sensors,

$$\langle N_i N_j^* \rangle = \delta_{ij} \cdot N_1 N_1^*$$ (3.24)

$$\delta_{ij} = \begin{cases} 0 & \text{if } i \neq j \\ 1 & \text{if } i = j. \end{cases}$$

Then the total power received by the array becomes

$$A = \frac{\langle \varsigma_1\varsigma_1^* \rangle \left[l + \sum_{i=1}^{l-1} \frac{1}{2}\left(l - i\right)cos(\omega\tau_i)\right] + l\langle N_1 N_1^* \rangle}{T}$$ (3.25)

Futhermore, if K is defined as

$$K = l + \sum_{i=1}^{l-1} \frac{1}{2}\left(l - i\right) cos(\omega \tau_i) \tag{3.26}$$

then equation 3.25 becomes

$$A = \frac{K\langle \varsigma_1 \varsigma_1^* \rangle + l\langle N_1 N_1^* \rangle}{T} \tag{3.27}$$

where equation 3.27 describes the array spectral density. Here, SNR_A describes the prevalence of the ambient noise and flow noise components of the array output, such that

$$\text{SNR}_A = \frac{K\langle \varsigma_1 \varsigma_1^* \rangle}{l\langle N_1 N_1^* \rangle} \tag{3.28}$$

Comparing equation 3.28 to the result derived for a single hydrophone, given by equation 3.12, we see that the beamformed array improves the signal-to-noise ratio by a factor of $\frac{K}{l}$. Furthermore, equation 3.28 suggests that array performance improves with an increasing number of hydrophones, l. For an array with 4 elements, at broadside, $\frac{K}{l} = \frac{7}{4}$.

3.3.7 Array Gain

The broadside beamforming analysis applied to the linear array generates a meaningful amount of artificial spectral density gain. As a result, an array gain formula is applied to the beamformed results to correct the inflated values. The array gain formula presented here is adapted from *Cox* (1973), such that

$$AG = 20 \log l \tag{3.29}$$

The array gain correction is performed by subtracting the result of equation 3.29 from the calculated array power spectral density (Equation 3.18).

3.3.8 Algorithm Assessment

Presently, equations 3.17 and 3.18 can be used to consolidate all channel signals into one array signal. Subsequent spectral slope analysis of the array spectral density, A, using equations 3.6 and 3.7 characterizes the prevalence of flow noise across the beamformed array. The resulting critical frequencies, f_c, of the coherent array can be compared to

the results of both spectral slope thresholding (single hydrophone) and spatial coherence thresholding to critically evaluate the relative performance of the beamformed array. Iterative spectral slope thresholding of different numbers of hydrophones quantifies the marginal benefit of additional hydrophones on an acoustical array.

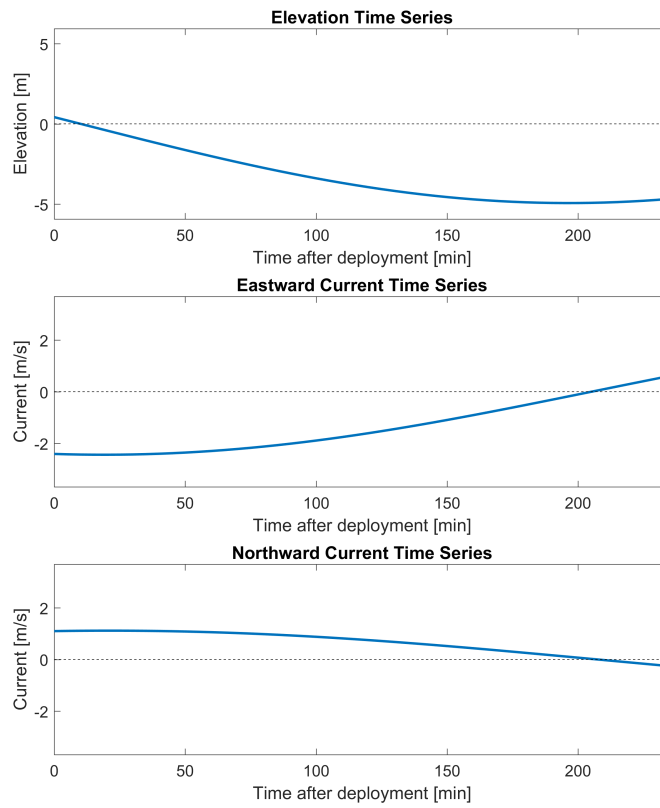# CHAPTER 4

RESULTS

4.1 Physical Conditions

Figure 4.1: Results from WebTide model over deployment period. Top panel is tidal elevation and bottom panels are current time series.

High resolution tidal data was generated using the Bedford Institute of Oceanography's WebTide, a tidal prediction model. The model outputs of interest are tidal elevation and tidal current speed, both of which are used to quantify the tidal conditions over the deployment period. The WebTide results for the experiment are shown in figure 4.1. The deployment period spans from maximum ebb tide (beginning of experiment) to slack tide (end of experiment), such that increasing elapsed time corresponds to decreasing flow speed.

4.2   Spectral Density

Power spectra were calculated for the entirety of the deployment period (Equation 3.2). The results show that spectral levels are elevated when flow is fast, and are diminished when flow is slow (Figure 4.2). The hydrophone spectral densities are partitioned into two distinct regions: a relatively loud, low-frequency section, and a relatively quiet, mid-to-high-frequency section. Signal levels are visibly elevated in high-flow conditions, indicating greater levels of flow noise, and are diminished as the flow speed, and therefore flow noise, is lessened. The mid-to-high-frequency band is less affected by this flow noise and is therefore comparatively quiet. Below 10 Hz there is a significant amount of noise, another sign of flow noise.

The hydrophone power spectra contain multiple episodes of mid-frequency noise. These signals are attributed to ship noise generated by the small vessel used in the guard buoy drifter tests, as outlined in section 3.2.3. Additionally, the abrupt shift in spectral densities at ~ 80 minutes is attributed to equipment reconfigurations.
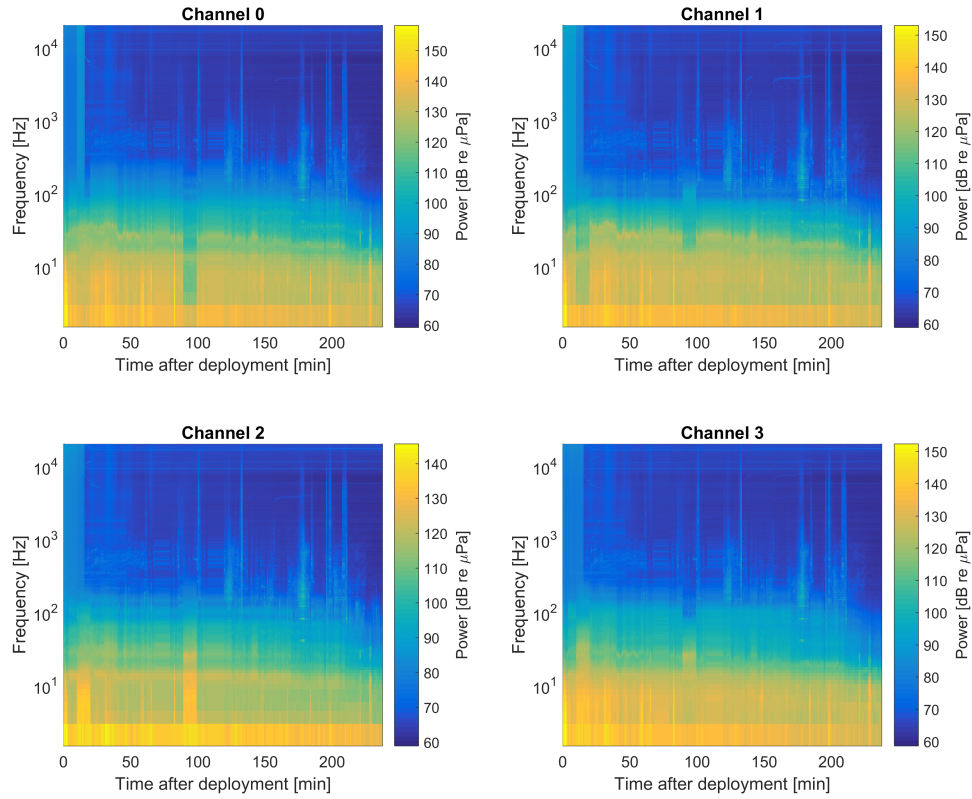
Figure 4.2: Power spectra for each hydrophone element on the array. Spectra are plotted over the deployment period across a range of low-to-mid frequencies. The spectra begin at maximum ebb tide and end at slack tide. Power decreases with flow speed over the deployment period.

Channel performance was assessed with a juxtaposition of individual channel power spectra, as shown in figure 4.3. A sensor's competence is determined by its relative levels across a range of frequencies. Visual comparison suggests that channels 1 and 2, the interior channels, consistently outperform channels 0 and 3, the exterior channels. The elements all show good agreement in spectral slopes and spectral shape across the frequencies of interest. Channel performance could be affected by the turbulent wake of leading hydrophones, a phenomenon discussed in *Barclay and Buckingham* (2013).

Figure 4.3 reveals that each element is subject to system noise above 1 kHz, indicated by a hard noise floor and the presence of electronic system noise above 10 kHz. As a result, the remaining spectral and coherence analyses disregard noise above 1 kHz.
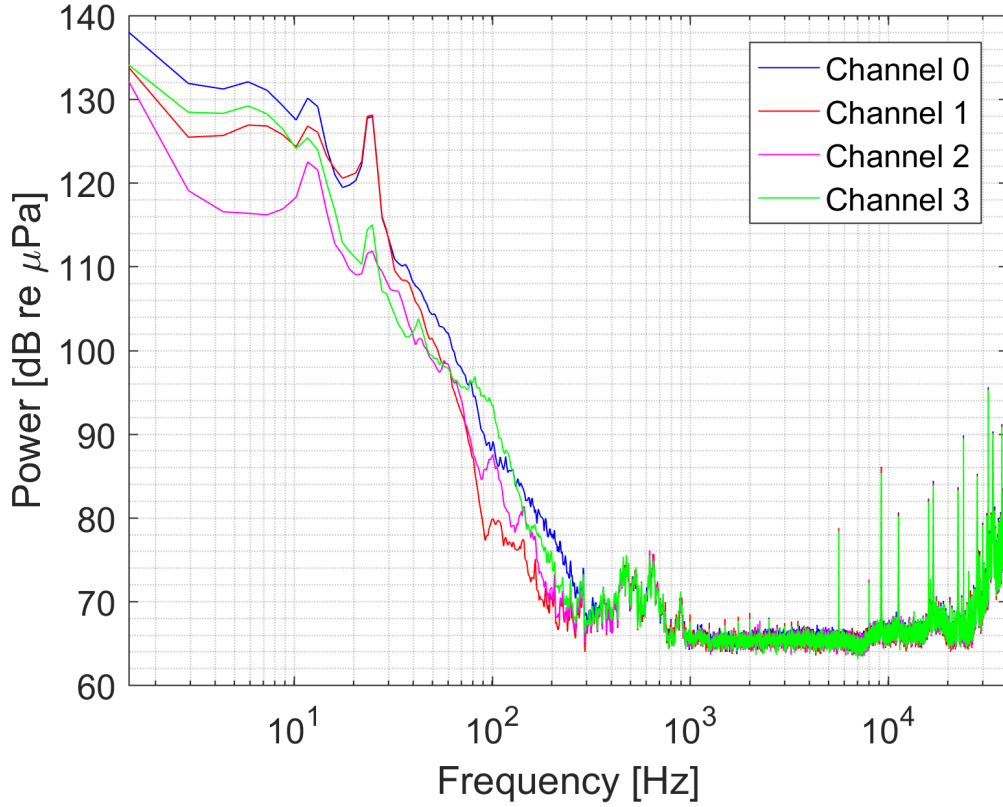
Figure 4.3: Signals recorded on each hydrophone 1.5 hr after deployment.

4.2.1 Power Spectrum Probability Density

The PSPD facilitates broad-scale assessment of a hydrophone's spectral density over the entire deployment period. The PSPD for each hydrophone on the array are shown in figure 4.4. Spectral densities are between 130 and 150 dB re μPa below 10 Hz, and between 70 to 90 dB re μPa at mid-to-high-frequencies.

Each channel follows a spectral slope of $f^{-5/3}$ at frequencies below 10 Hz, behaviour analogous to Kolmogorov's turbulence theory. This spectral slope is a symptom of turbulence interacting with the array, and indicates a region of flow noise. A steepened spectral slope of f^{-m}, where $m > \frac{5}{3}$, persists between 10 to 100 Hz, a result of small-scale turbulence where turbulence wavelength $<<$ sensor size. This small-scale turbulence is averaged out over the surface of the hydrophone sensor, effectively dampening the measured signals. Lastly, the PSPD results show that ambient noise is dominant above 300 Hz, where signal levels are markedly low. The electronic system noise floor previously identified in figure 4.3 is also present here. The hard noise floor is at about 60 dB re μPa.

The PSPD supports the identification of sound-sources from the experimental period. For example, the PSPD results reveal that a number of signals contain an artificial noise floor (~ 80 dB re μPa), a product of electronic system noise recorded by the array sensors. While this electronic noise is quite blatant in the PSPD results, its brevity makes it difficult to identify in figure 3.2. Signals superimposed on the PSPD suggest that measurements in slow current conditions contain a greater extent of ambient noise over frequency relative to those in fast current conditions.
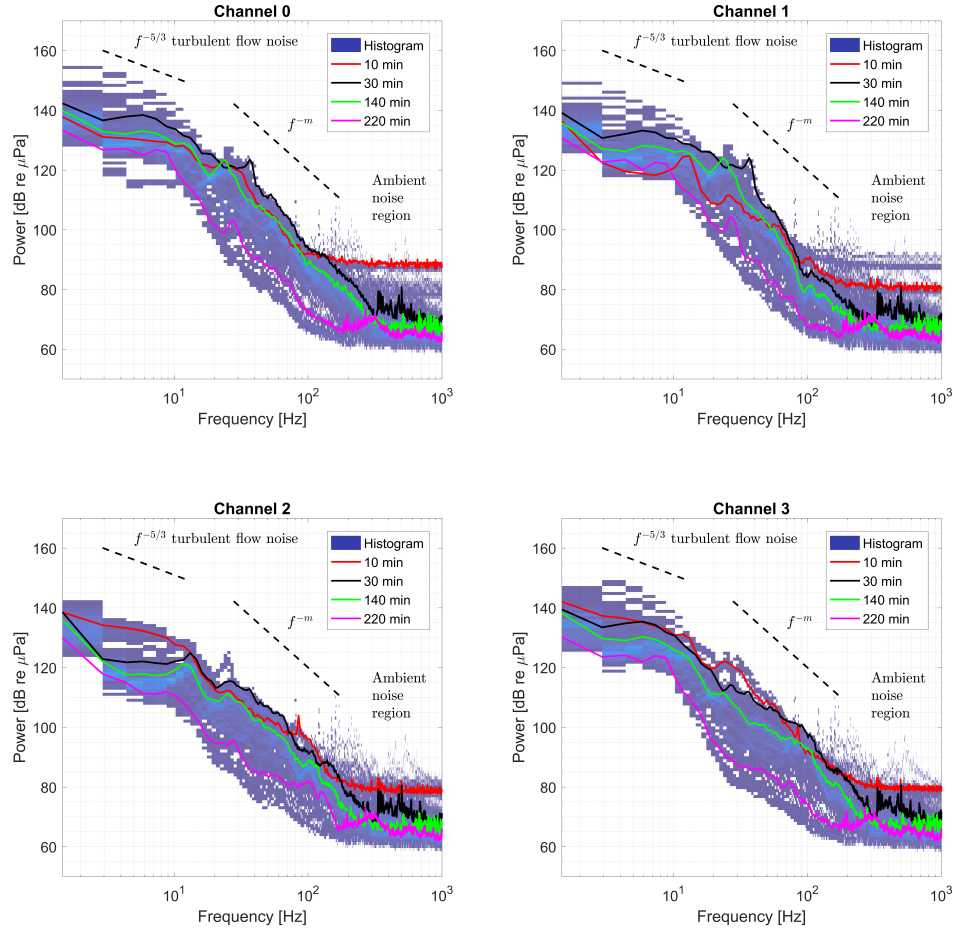

Figure 4.4: Power spectrum probability density for the entire deployment period on each channel. Turbulent flow noise is prevalent < 10 Hz (where wavelengths $>>$ sensor size), with a spectral slope of $f^{-5/3}$, while turbulent flow noise interacting with a hydrophone's finite size (in the 10 Hz to 100 Hz band) yields a spectral slope of f^{-m}. The ambient sound field dominates at ~ 300 Hz.
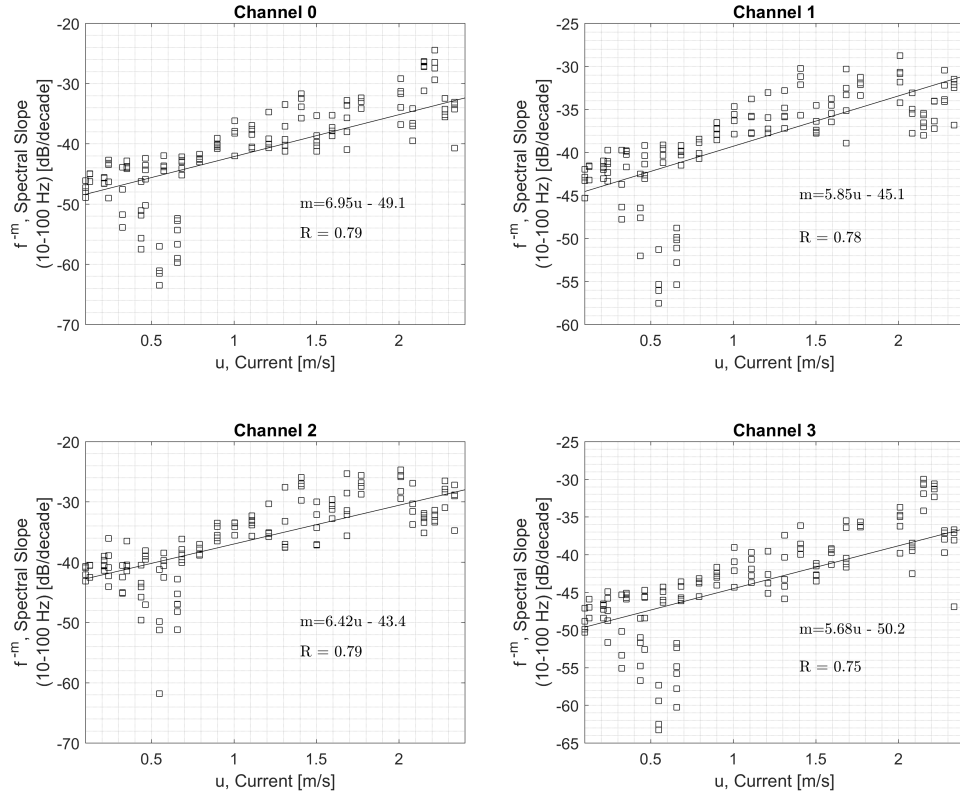
4.2.2   Spectral Slope Thresholding

Figure 4.5: Current speed dependence on flow noise spectral slopes, m. Spectral slope magnitude increases with decreasing flow. Spectral slope magnitudes remain greater than Knudsen's theoretical -17 dB./decade. Spectral slopes, f^{-m}, are between 10 and 100 Hz. Correlation coefficients, R, are reported.

Equation 3.6 was used to iteratively calculate the spectral slope between 10 and 100 Hz, f^{-m}. The spectral slopes were linearly regressed against their respective current conditions, as shown in figure 4.5. The relationship between spectral slope, f^{-m}, and current speed indicates that signals recorded decreasing current conditions are increasingly dampened. The correlation coefficients, R, are reported for each fit to quantify the linear fit between current and spectral slope. Evidently, the spectral slope and current speed are highly correlated.

Theories from Kundsen and Kolmogorov suggest that the spectral slope of -17 dB/decade corresponsds to wind-generated and turbulence-generated noise, respectively. The

spectral slopes observed between 10 and 100 Hz, f^{-m}, range from -25 to - 60 dB/decade, considerably steeper than -17 dB/decade. The relationship between spectral slope and flow speed holds for currents as quick as 2.5 m/s.
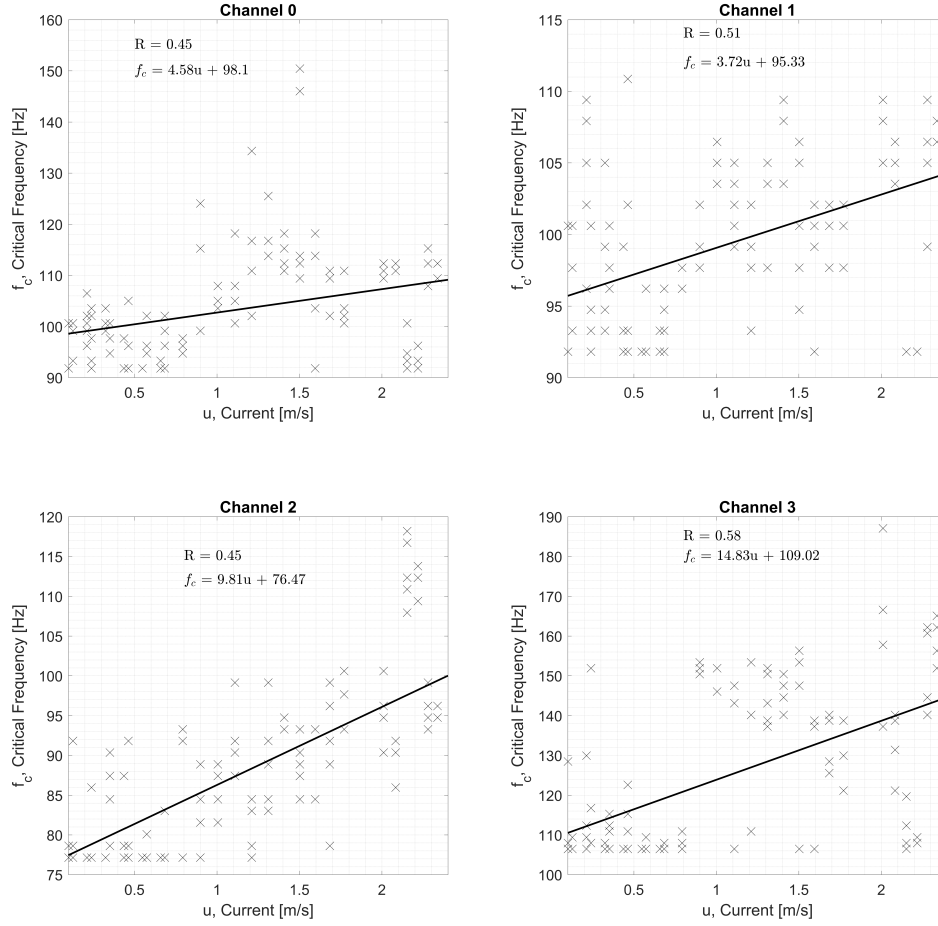

Figure 4.6: Current speed dependence of critical frequency, f_c, as defined in equation 3.7. Critical frequency reveals where flow noise is no longer dominant. Correlation coefficients, R, are reported.

The critical frequency (frequency at which flow noise and ambient noise are equal in power) was iteratively calculated over the experimental period using equation 3.7. The critical frequencies were linearly related to their respective current conditions, as shown in figure 4.6. There is a positive correlation between critical frequency and current speed, where fast flow coincides with high critical frequencies. Critical frequency is a quantitative

indicator of flow noise prevalence, where higher critical frequencies imply more pervasive flow noise. As such, the spectral slope critical frequency method is used to track the transition from the flow noise region to the ambient noise region.

The linear relationship between spectral slope critical frequency and current speed is ascertained with the correlation coefficient, R. As the results show, the correlation is significant, though disagreement between the fit for each channel is large since outliers are included in the regressions. Importantly, the intercepts has not been forced to zero. This is because it is unrealistic to expect that we can rid the system completely of flow noise, or low-frequency noise generated by the mechanical systems that comprise the tow body. If this were a moored system with no surface expression, that assumption might be valid, but is not considered here.

4.3   Spatial Coherence

Spatial coherence is calculated for different hydrophone combinations across the linear array using equation 3.3. The spatial coherence results are presented in magnitude coherence for the entire deployment period over a range of frequencies (Figure 4.7). Coherence is a measure of the similarity between the signals recorded on two hydrophones.

One important feature of the spatial coherence results relates to the relationship between wavelength and hydrophone co-location. If the wavelength of propagating sound is sufficiently large the sensors would become relatively co-located. That is to say, large-wavelength sound would generate high coherence between proximal elements. However, the results suggest that the low frequency data is overwhelmingly incoherent. This implies that uncorrelated flow noise is eroding this wavelength-coherence relationship, since the locally generated flow noise is incoherent across the array.

Flow noise is inherently stochastic and propagating ambient noise is highly correlated at low frequencies (relative to hydrophone spacing). As a result, low coherence and high coherence are a sign of flow noise and ambient noise, respectively. Therefore, the spatial coherence results are partitioned into two distinct regions: a flow noise region and an ambient noise region. A stark boundary exists between these two noise regions. Visual assessment suggests that flow noise is consistently present at low frequencies and can be prominent at higher frequencies (above 600 Hz) if hydrophone separation distance is sufficient. The ambient noise region is present between 200 and 600 Hz and contains the

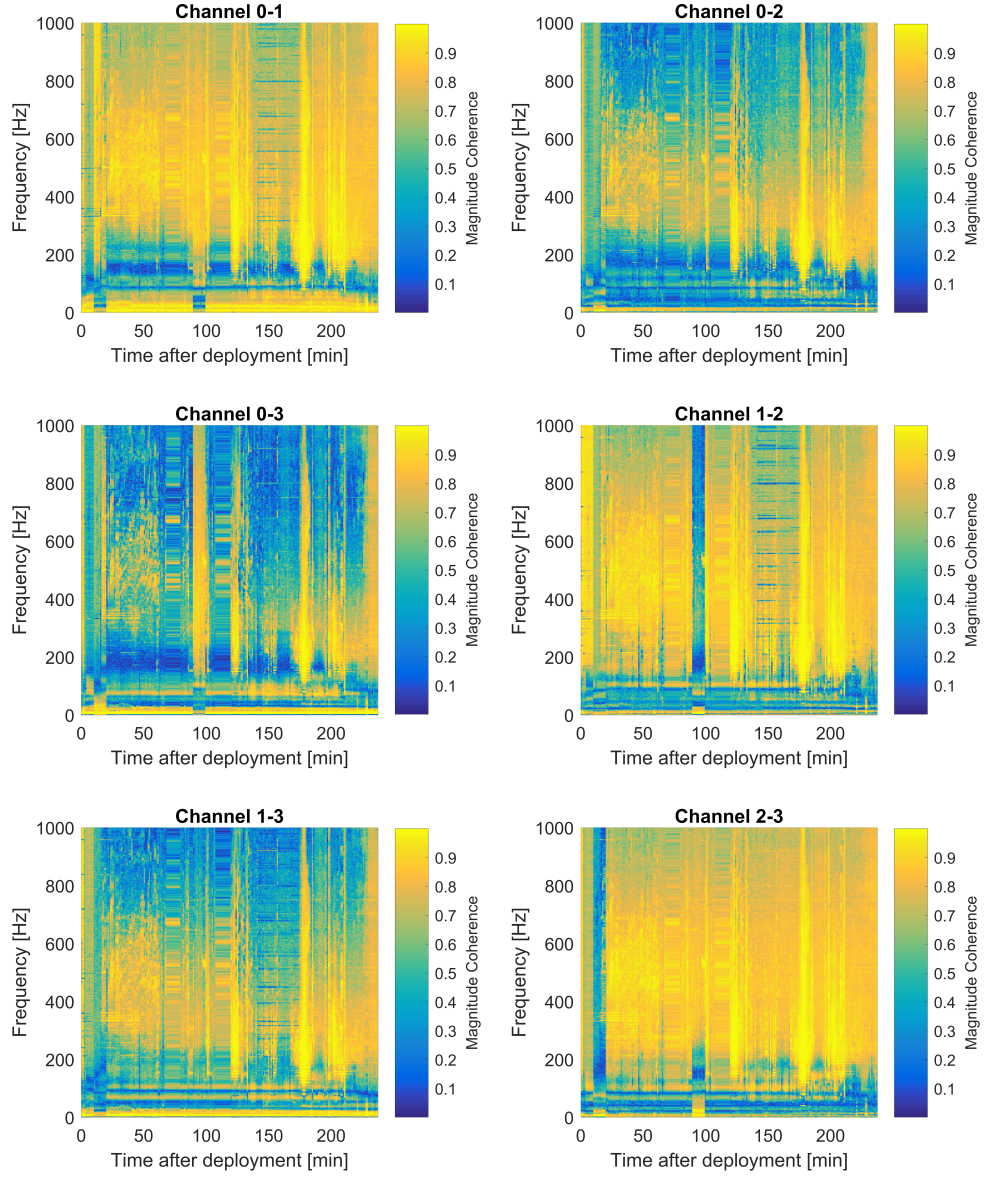same vessel noise observed in figure 3.2.

Figure 4.7: Channel spatial coherence over the experimental period. Magnitude coherence is expected to tend to unity as the hydrophones become relatively co-located. However, uncorrelated flow noise on each phone breaks that relationship. Incoherent flow noise regions decrease as current speed slows.

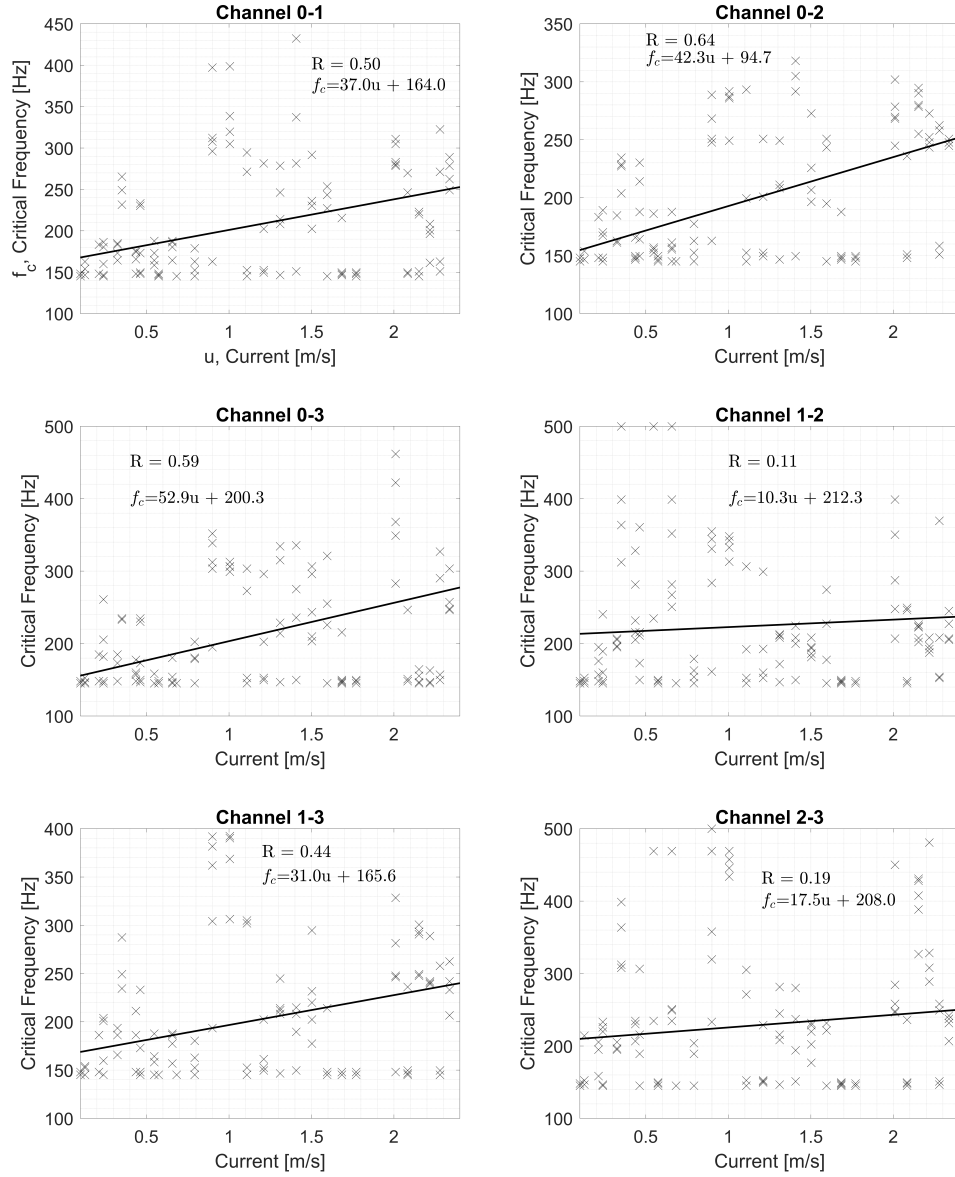## 4.3.1 Spatial Coherence Threshold

Figure 4.8: Current dependency of spatial coherence threshold. Spatial coherence threshold used to detect the critical frequency in a more precise way than the spectral sloping method.

The spatial coherence critical frequency is the frequency at which the boundary between the ambient noise and flow noise regions occurs (Equation 3.8). The spatial coherence

critical frequency was iteratively calculated for each combination of channels, and is used to quantify the relative prevalence of flow noise and ambient noise within a measurement (Figure 4.8). The spatial coherence critical frequency is a more rigorous method of flow noise measurement than the spectral sloping critical frequency, as spatial coherence is an indicator of flow noise *cessation* rather than noise region *transition*. The spatial coherence critical frequency increases with increasing flow speed, a relationship similar to that of the spectral slope critical frequency.

It is important to note that the coherence is impacted by any temporary deterministic noises present in the sound field, such as the auxiliary RHIB, mechanical array noise, or noise generated aboard the Nova Endeavour. In such instances, the automated critical frequency detector fails, and yields an outlier. Such outliers could be the source of the low correlation between channels 1-2 and 2-3.

There is a good deal of noise in figure 4.8, as no outliers nor oddities were discarded. The retention of outliers is done to maintain the integrity of the linear regression. This makes the regression statistically rigorous and suggests that the correlation is a meaningful one.

4.4   Beamforming

The beamforming algorithm applied across the array is defined in in equation 3.18, and generates an array power spectrum that can be analyzed using equation 3.7 to identify the spectral slope critical frequencies of the coherent array. The coherent array critical frequency, average spectral critical frequency, and average coherence critical frequency distributions were regressed against current conditions, as shown in figure 4.9. The shaded sections around each critical frequency regression shows the standard deviation of each critical frequency method. The standard deviations of the spectral slope and spatial coherence critical frequency regressions were extracted from the averaged fits, while the standard deviation of the coherent array critical frequency regression was calculated from the data during the regression.

The spatial coherence critical frequency identification method yields relatively high threshold/transition frequencies, while the single hydrophone and coherent array spectral slope critical frequencies are at relatively low frequencies. This is attributed to the rigorous and precise nature of the spatial coherence thresholding method, which signifies the

cessation of flow noise. That is, above this line we can be confident that there is no contamination of the ambient noise field by flow noise. Conversely, the single hydrophone and coherent array thresholds only show where the noise regime transitions from flow noise to ambient noise. The critical frequency regressions/distributions serve as upper and lower bounds of different noise regimes. Importantly, the coherent array contains significantly lower critical frequencies than the single hydrophone, indicating that the broadside beamforming approach lessens the extent of flow noise on the measurements.
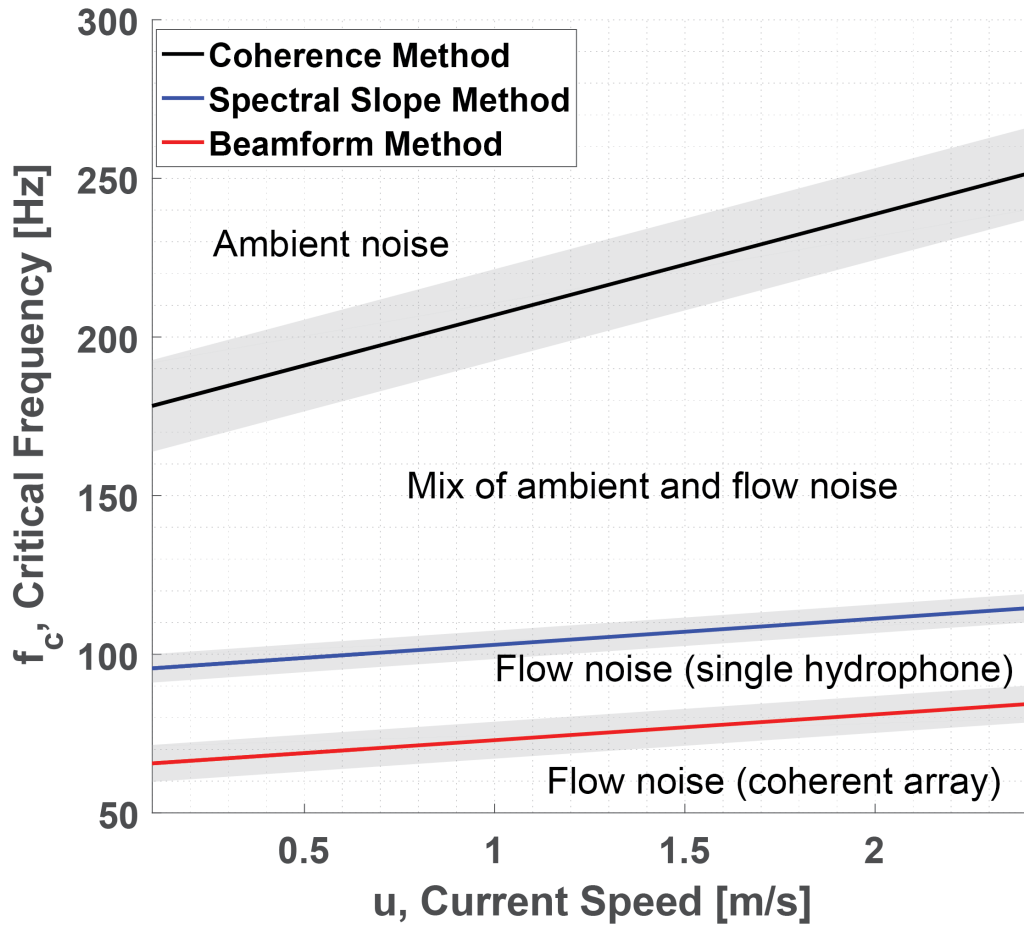
Figure 4.9: Comparison of hydrophone spectral slope, coherence threshold, and array spectral slope critical frequency identification methods. Coherence and spectral analysis reveal regions of flow, ambient, and mixed noise. Uncertainties are standard deviation (shaded).

Consideration of the power spectra of the coherently averaged array facilitates the visual

assessment of the performance of the beamforming algorithm described in equation 3.18. Figure 4.10 compares guard buoy, single hydrophone, and coherent array power spectra at 1.5 hours into the experiment. Different combinations of hydrophone numbers are processed with the beamforming algorithm to evaluate the marginal acoustical benefits of adding hydrophones to an array.

The guard buoy spectrum is selected based on the drifter's distance from the *MV Nova Endeavour* and the timestamps of each transect. We select a time where the drifter and array were in close proximity (i.e. separation distance minimum) to establish a meaningful comparison. The separation distance is visualized in figure 4.11.
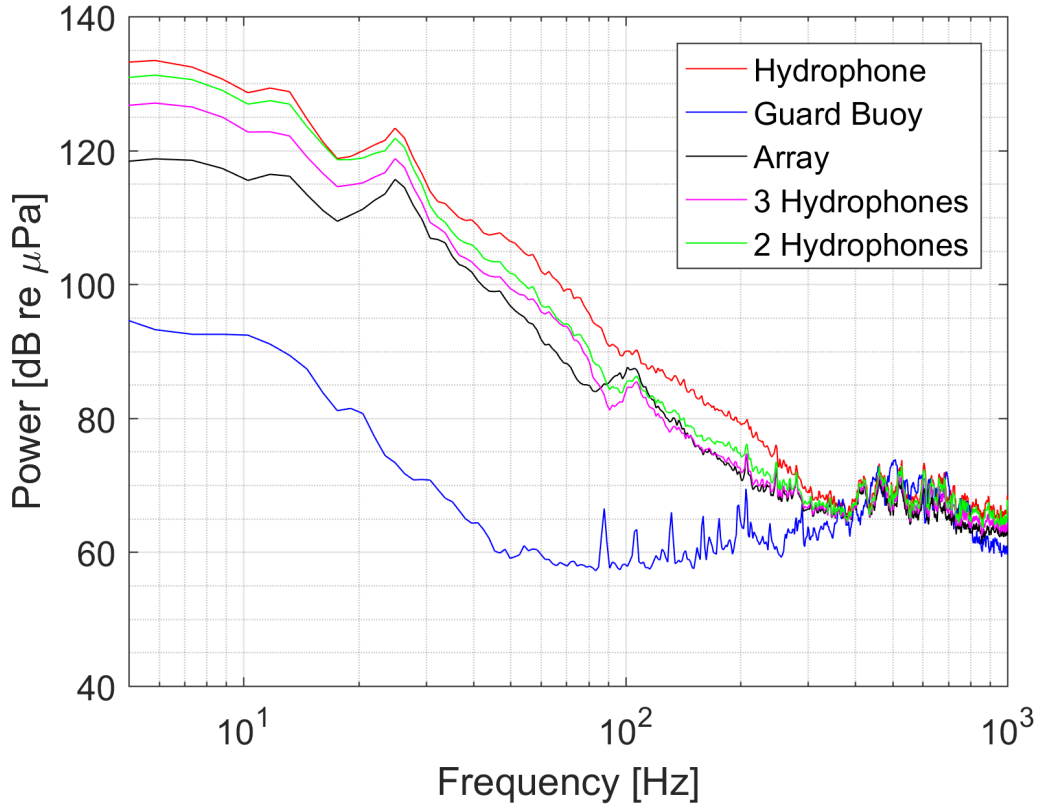

Figure 4.10: Comparison of hydrophone, coherent array, and guard buoy signals captured at 1.5 hr into the deployment.

The guard buoy spectrum behaves differently from the rest, exhibiting significantly lower levels at frequencies below 100 Hz. A frequency shoulder, or pronounced excursion in spectral slope, is present at 10 Hz in the guard buoy spectrum, suggesting non-negligible

flow noise is affecting the guard buoy measurements. This is typical of all moored or free drifting passive acoustic systems that have a surface expressions or subsurface float. The single hydrophone shows pointed effects of flow noise at low frequencies.

The spectra reveal that the coherent array spectra transitions to the ambient noise region at lower frequencies than the other hydrophone combinations (excluding the guard buoy). Furthermore, there exists a sequential hydrophone-critical frequency relationship, where adding hydrophones lowers the measured signal levels below the critical frequency. This is evidenced by the downward shift in signal power frequency as more hydrophones are averaged/beamformed. There is reasonable agreement between the guard buoy and coherent array above the critical frequency, with some difference above 700 Hz. This disparity is attributed to the lack of co-location between the array and the guard buoy, as they are vertically and horizontally displaced relative to each other. Importantly, coherent averaging across the array does not seem to jeopardize signal variability.
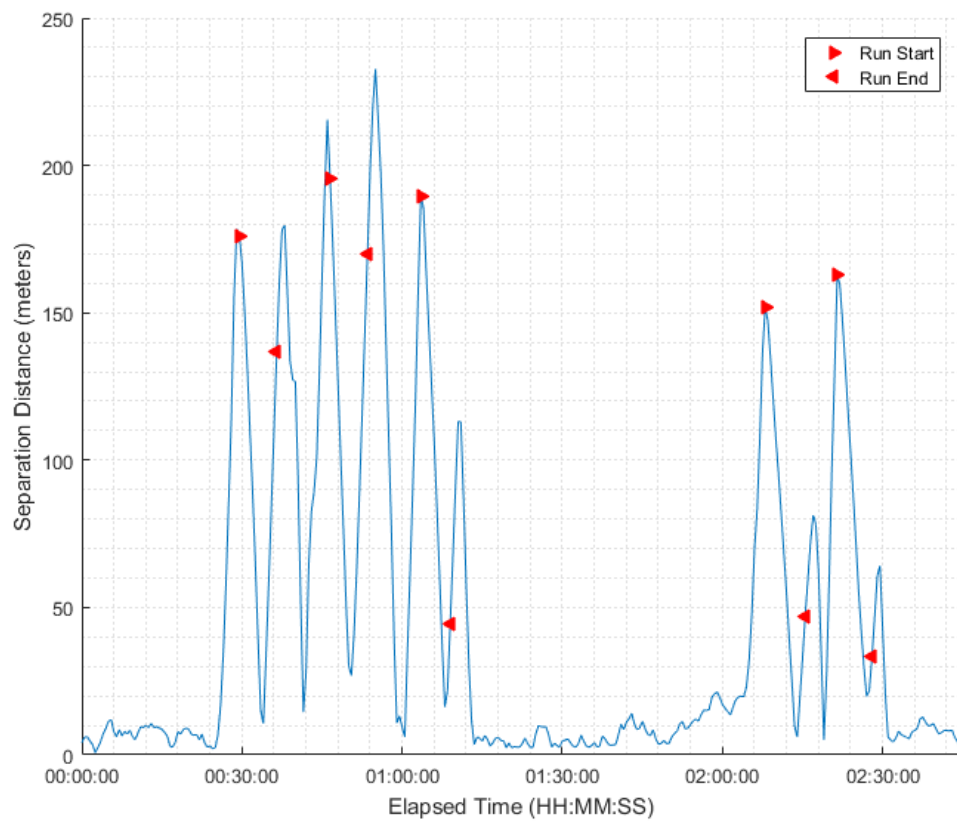
Figure 4.11: Separation distance between the guard buoy and *MV Nova Endeavour*. Red arrows indicate the start and end of a transect.

CHAPTER 5

DISCUSSION

5.1   Spectral Slope Thresholding

Iterative calculations of spectral slopes between 10 and 100 Hz, f^{-m}, were regressed against current speed. The resulting spectral slopes are far steeper than the theoretical slope of $f^{-5/3}$, which corresponds to wind or turbulence sound sources. These steepened slopes are a result of the averaging out of small-scale turbulence over the sensors, and have previously been identified by both *Lombardi* (2016) and *Bassett et al.* (2014). There is visible interchannel variability in the relationship between the spectral slope and local current conditions. This is a result of the mechanical nature of the array and its interaction with fluid flow - as phones placed at different parts along the array have small but non-negligible differences in their interaction with the turbulent flow. Additionally, the natural randomness of turbulence would lend itself to the different linear relationships observed. Nonetheless, there is a strong relationship between spectral slope and flow speed.

These spectral slopes were used in equation 3.7 to identify critical frequency and quantify the prevalence of flow noise within a measured signal. Results show that critical frequency and flow speed are positively related, indicating that flow noise is prevalent in fast current conditions. This is intuitive, as flow noise and current speed are intimately related. The spectral slope critical frequency presents a new method of identifying the transition region between flow noise and ambient noise. As such, the spectral slope critical frequency results could lead to improvements in flow noise models, and contribute to our ability to predict the shape and levels of flow noise in a tidal channel.

Spectral slope critical frequencies describe the transition from a flow noise region to an ambient noise region. The nature of this transition region provides two important insights.

Firstly, frequencies above the critical frequency will contain a mixture of ambient noise and flow noise, since the threshold merely marks the *reduction* in flow noise, and not the *absence*. Secondly, frequencies below the critical frequency will exclusively contain flow noise, since the spectral slopes correspond to turbulence theory. These insights are important, as they provide useful context for future signal level and sound-source evaluations in tidal channel measurements.

5.2   Spatial Coherence

Spatial coherence evaluates the agreement between two sensors. Spatial coherence results for different sensor combinations show that there are two distinct coherence regions across the array: an incoherent flow noise region and a coherent ambient noise region. The prevalence of these regions is quantified with the spatial coherence thresholding described in equation 3.8. Iterative calculations of the spatial coherence critical frequency were regressed against current speed. There is a positive relationship between spatial coherence critical frequency and current speed, similar to the spectral slope thresholding method. The spatial coherence critical frequency facilitates the identification of the cessation of flow noise within a signal. That is, the spatial coherence critical frequency marks the boundary between pure ambient noise and a mixture of ambient and flow noise.

These results are linked to the spectral sloping critical frequencies such that the spectral slope method provides a lower boundary, below which only flow noise exists, and the spatial coherence method provides an upper boundary, above which only ambient noise exists. Intermediate frequencies correspond to a mixture of flow noise and ambient noise. This explains why the spatial coherence critical frequencies are markedly higher than those of the spectral sloping method. The application of spectral slope and spatial coherence critical frequencies provides valuable insight on the relative extent of both ambient noise and flow noise within a signal.

5.3   Beamforming

By effectively treating the array as one sensor or hydrophone, signal processing can address the pseudo-sound plaguing low frequency data. Coherently averaging hydrophones suppresses uncorrelated data and enhances the measurement of common signatures. Thus,

coherent averaging will suppress stochastic flow noise and enhance the detection of propagating ambient noise. The coherent averaging employs a broadside approach with no steering angle, and is outlined in equation 3.18.

The result of the broadside beamforming is a coherent array spectrum, not unlike figure 4.2. Application of spectral slope thresholding (Equation 3.7) to the coherent array spectrum reveals that the broadside beamforming has a substantial effect on the noise composition of the array spectra. These results are visualized in figure 4.9, and show how the coherent array contains lower levels and lower critical frequencies than the single hydrophone (Figure 4.10). This implies that the coherent array is less affected by flow noise, and contains a greater extent of ambient noise. A sequential relationship arises between array performance and the number of elements on the array, such that an increasing number of elements improves signal levels below the critical frequency. As such, a larger and more populated array is expected to further suppress a measurement's flow noise components.

CHAPTER 6

CONCLUSIONS

Recall the objectives of this study:

1. Use spectral analysis and spatial coherence to identify and characterize flow noise at low frequencies.

2. Use beamforming and coherent averaging to improve the performance of the array by suppressing flow noise and enhancing the measurement of ambient noise.

In light of the results and findings presented in the preceding sections, we can conclude that:

1. Flow noise appears in two regions: as the theoretical $f^{-5/3}$ noise when wavelength $>>$ sensor size, and as an f^{-m} sloped process, where the sensor's finite dimension reduces the flow noise at relatively higher frequencies. f^{-m} is related to the flow speed over the array. The spectrum's deviation from f^{-m} slope indicates where flow noise is no longer dominant. Spatial coherence can be used to identify when effect of flow noise is negligible.

2. Coherent processing (beamforming) suppresses flow noise and yields a lower critical frequency at all flow speeds than that of a single hydrophone. An increased number of hydrophones and array length would improve array performance allowing passive acoustic monitoring at arbitrarily low frequencies.

BIBLIOGRAPHY

Alsarayreh, T., and L. Zedel, Quantifying snowfall rates using underwater sound, *Atmosphere-Ocean*, *49*, 61–66, 2011.

Bailey, H., B. Senior, D. Simmons, J. Rusin, G. Picken, and P. M. Thompson, Assessing underwater noise levels during pile-driving at an offshore windfarm and its potential effects on marine mammals, *Marine Pollution Bulletin*, *60*, 888–897, 2010.

Barclay, D. R., and M. J. Buckingham, Depth dependence of wind-driven, broadband ambient noise in the philippine sea, *The Journal of the Acoustical Society of America*, *133*, 62–71, 2013.

Bassett, C., J. Thomson, P. H. Dahl, and B. Polagye, Flow-noise and turbulence in two tidal channels, *The Journal of the Acoustical Society of America*, *135*, 1764–1774, 2014.

Carey, W. M., and D. Browning, Low frequency ocean ambient noise: measurements and theory, in *Sea Surface Sound*, pp. 361–376, Springer, 1988.

Cato, D. H., Ocean ambient noise: Its measurement and its significance to marine animals, *Proc. Inst. Acoustics*, *30*, 1–9, 2008.

Cox, H., Line array performance when the signal coherence is spatially dependent, *The Journal of the Acoustical Society of America*, *54*, 1743–1746, 1973.

Croll, D. A., C. W. Clark, J. Calambokidis, W. T. Ellison, and B. R. Tershy, Effect of anthropogenic low-frequency noise on the foraging ecology of balaenoptera whales, *Animal Conservation*, *4*, 13–27, 2001.

Dadswell, M. J., Occurrence and migration of fishes in minas passage and their potential for tidal turbine interaction, 2010.

Dushaw, B., W. Au, A. Beszczynska-Möller, R. Brainard, B. D. Cornuelle, T. Duda, M. Dzieciuch, E. Fahrbach, A. Forbes, L. Freitag, et al., A global ocean acoustic observing network, *Proceedings of OceanObs 09: Sustained Ocean Observations and Information for Society*, *2*, 2010.

Franz, G., Splashes as sources of sound in liquids, *The Journal of the Acoustical Society of America*, *31*, 1080–1096, 1959.

Gaul, R. D., D. P. Knobles, J. A. Shooter, and A. F. Wittenborn, Ambient noise analysis of deep-ocean measurements in the northeast pacific, *IEEE Journal of Oceanic Engineering*, *32*, 497–512, 2007.

Gordon, D. C., Intertidal ecology and potential power impacts, bay of fundy, canada, *Biological Journal of the Linnean Society*, *51*, 17–23, 1994.

Gordon, J., D. Gillespie, J. Potter, A. Frantzis, M. P. Simmonds, R. Swift, and D. Thompson, A review of the effects of seismic surveys on marine mammals, *Marine Technology Society Journal*, *37*, 16–34, 2003.

Halvorsen, M., T. Carlson, and A. Copping, Effects of tidal turbine noise on fish hearing and tissues, *Pacific Northwest National Laboratory technical report, PNNL-20786*, 2011.

Hildebrand, J. A., Anthropogenic and natural sources of ambient noise in the ocean, *Marine Ecology Progress Series*, *395*, 5–20, 2009.

Ingenito, F., and S. Wolf, Site dependence of wind-dominated ambient noise in shallow water, *The Journal of the Acoustical Society of America*, *85*, 141–145, 1989.

Jensen, F. B., W. A. Kuperman, M. B. Porter, and H. Schmidt, *Computational ocean acoustics*, Springer Science & Business Media, 2000.

Karsten, R. H., J. McMillan, M. Lickley, and R. Haynes, Assessment of tidal current energy in the minas passage, bay of fundy, *Proceedings of the Institution of Mechanical Engineers, Part A: Journal of Power and Energy*, *222*, 493–507, 2008.

Khan, M., G. Bhuyan, M. Iqbal, and J. Quaicoe, Hydrokinetic energy conversion systems and assessment of horizontal and vertical axis turbines for river and tidal applications: A technology status review, *Applied energy*, *86*, 1823–1835, 2009.

Knudsen, V. O., R. Alford, and J. Emling, Underwater ambient noise, *J. Mar. Res.*, *7*, 410–429, 1948.

Lighthill, M., The bakerian lecture, 1961. sound generated aerodynamically, in *Proceedings of the Royal Society of London A: Mathematical, Physical and Engineering Sciences*, vol. 267, pp. 147–182, The Royal Society, 1962.

Lombardi, A., Soundscape characterization in grand passage, nova scotia, a planned in-stream tidal energy site, 2016.

Ma, B. B., and J. A. Nystuen, Passive acoustic detection and measurement of rainfall at sea, *Journal of atmospheric and oceanic technology*, *22*, 1225–1248, 2005.

Merchant, N. D., T. R. Barton, P. M. Thompson, E. Pirotta, D. T. Dakin, and J. Dorocicz, Spectral probability density as a tool for ambient noise analysis, *The Journal of the Acoustical Society of America*, *133*, EL262–EL267, 2013.

Minnaert, M., Xvi. on musical air-bubbles and the sounds of running water, *The London, Edinburgh, and Dublin Philosophical Magazine and Journal of Science*, *16*, 235–248, 1933.

Morrison, K. J., and A. M. Redden, Bottom substrate and associated epibenthic biota of the force tidal energy test site in the minas passage, bay of fundy, Ph.D. thesis, Acadia University, 2012.

Mulligan, P., Bay of fundy tidal turbine battle opens in halifax courtroom, 2017.

Patrício, S., A. Moura, and T. Simas, Wave energy and underwater noise: State of art and uncertainties, in *OCEANS 2009-EUROPE*, pp. 1–5, IEEE, 2009.

Prosperetti, A., Bubble-related ambient noise in the ocean, *The Journal of the Acoustical Society of America*, *84*, 1042–1054, 1988.

Shaw, J., B. J. Todd, M. Z. Li, and Y. Wu, Anatomy of the tidal scour system at minas passage, bay of fundy, canada, *Marine Geology*, *323*, 123–134, 2012.

Smith, J. W., and B. C. Pijanowski, Human and policy dimensions of soundscape ecology, *Global Environmental Change*, *28*, 63–74, 2014.

Strasberg, M., Nonacoustic noise interference in measurements of infrasonic ambient noise, *The Journal of the Acoustical Society of America*, *66*, 1487–1493, 1979.

Tollit, D., J. Wood, J. Broome, and A. Redden, Detection of marine mammals and effects monitoring at the nspi (openhydro) turbine site in the minas passage during 2010, *Report to Fundy Ocean Research Centre for Energy*, 2011.

Vagle, S., W. G. Large, and D. M. Farmer, An evaluation of the wotan technique of inferring oceanic winds from underwater ambient sound, *Journal of atmospheric and oceanic technology*, *7*, 576–595, 1990.

Van Dyke, M., *An album of fluid motion*, vol. 176, Parabolic Press Stanford, 1982.

Wenz, G. M., Acoustic ambient noise in the ocean: Spectra and sources, *The Journal of the Acoustical Society of America*, *34*, 1936–1956, 1962.

Wilson, B., R. S. Batty, and L. M. Dill, Pacific and atlantic herring produce burst pulse sounds, *Proceedings of the Royal Society of London B: Biological Sciences*, *271*, S95–S97, 2004.

Wilson, E., An assessment of coastal erosion in the minas basin, nova scotia, 2016.